Investigation of Quasi-Static And Dynamic Mechanical Properties of Functionally Graded Sic-Particulate Reinforced Aluminium Metal Matrix Composites

By

Uygar YILDIRIM

A Dissertation Submitted to the
Graduate School in Partial Fulfillment of the
Requirements for the Degree of

MASTER OF SCIENCE

Department: Mechanical Engineering
Major: Mechanical Engineering

İzmir Institute of Technology
İzmir, Turkey

August, 2004

We approve the thesis of **Uygar YILDIRIM**

Date of Signature

20.08.2004

Assoc. Prof. Dr. Mustafa GÜDEN
Supervisor
Department of Mechanical Engineering

20.08.2004

Assist. Prof. Dr. H. Seçil ARTEM
Department of Mechanical Engineering

20.08.2004

Assist. Prof. Dr. Engin AKTAŞ
Department of Civil Engineering

20.08.2004

Assoc. Prof. Dr. Barış ÖZERDEM
Head of Department

ACKNOWLEDGEMENT

ABSTRACT

Functionally Graded Material (FGM) systems composing of SiC-particulate reinforced Al Metal Matrix Composites (MMCs) of varying reinforcement volume fractions were prepared using a powder metallurgy route and investigated for mechanical properties under compression at quasi-static and high strain rates. High strain rate tests in the range of 1000-3000s-1 were conducted using a compression type Split Hopkinson Pressure Bar (SHPB) set-up.

The compression true stress-strain curves of the tested elastic-plastic FGM systems were satisfactorily approximated using the equal-stress model while the high strain rate testing in SHPB involved complex wave propagation events between the layers of FGM. The samples failed under compression at high strain rates particularly at the interface of the layer of the lowest impedance. This result was also confirmed with LSDYNA3 finite element modeling of a 10 and 20% SiC layered composite material system. The model has shown that higher compressive stress-time history occurred in the layer of the lowest impedance during SHPB testing.

Microscopic observation of the failed samples was further shown that the mechanically weakest link of the layered samples was the interfaces between the layers. This was solely due to the formation of a thin oxide layer at the interfaces. The modeling results were further found to be promising in modeling of FGM systems for future investigations.

CHAPTER 1   ÖZ

Değişen takviye hacim oranlarına sahip SiC parçacık takviyeli Al matriks Metal Matriks Kompozitlerden (MMK) oluşan Fonksiyonel Dereceli Malzemeler (FDM), toz metalurjisi yöntemiyle hazırlanarak, statik ve dinamik yükler altındaki ezilme davranışları incelenmiştir. Dinamik testler basma tipi Split Hopkinson Basınç Çubuğu (SHBÇ) kullanılarak 1000-3000s^{-1} aralığında yapılmıştır.

Test edilen elastik-plastik FDM sistemlerinin gerçek gerilme-genleme eğrileri eşit gerilme yöntemi kullanılarak tahmin edilebilirken, SHBÇ ile yapılan dinamik testler FDM nin katmanları arasında kompleks dalga yayılmaları göstermiştir. Numuler yüksek hızlarda yapılan dinamik basma testlerinde özellikle, empedansı en düşük olan katmanın ara yüzeyinden kırılmıştır. Bu sonuç, %10 ve %20 SiC katmanlı kompozit malzeme sisteminin LSDYNA-3 kullanılarak yapılan sonlu elemanlar modeliyle de doğrulanmıştır. Modelleme sonucunda, dinamik basma testleri esnasında en düşük empedansa sahip katmanın daha yüksek basma gerilme-zaman geçmişine sahip olduğu görülmüştür.

Kırılan numunelerin mikroskobik olarak incelenmesi, katmanlı numunelerde mekanik olarak en zayıf bağın katmanlar arasındaki ara yüzeyler olduğunu göstermiştir. Bunun tek nedeni ara yüzeylerde ince bir oksit tabakasının oluşmasıdır. Modelleme sonuçları, FDM sistemlerinin ileriki araştırmalar için modellenmesinde umut vermektedir.

TABLE OF CONTENTS

LIST OF FIGURES

LIST OF TABLES

CHAPTER 2

INTRODUCTION

Recent advances in materials processing and engineering have led to a new class of materials called Functionally Graded Materials (FGMs). FGMs display continuously or discontinuously (discretely) (Figures 1.1(a) and (b) varying compositions and/or microstructures and related properties including hardness, density, thermal conductivity, resistance, Young's modulus and etc., over definable geometrical distances according to the desired function. The gradients can be continuous on a microscopic level, or they can be laminates comprised of gradients of metals, ceramics, polymers, or variations of porosity/density.

(a)

(b)
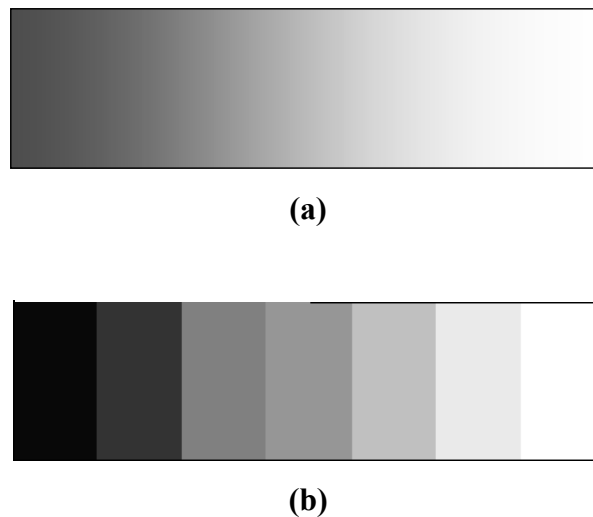
Figure 1.1 Gradient architecture of FGMs; (a) continuously graded and (b) discretely layered FGMs.

The history of FGMs may be dated back to 80s. The initial idea of a graded material was to combine the incompatible properties of heat resistance and toughness with low internal thermal stress, by producing a compositionally graded structure of distinct ceramic and metal phases [1]. In 1987 a large national project entitled, *Research on the Basic Technology for the Development of Functionally Gradient Material for Relaxation of Thermal Stress*, commenced in Japan. The project was aimed at developing superheat-resistant materials for the propulsion system and air-

frame of the space plane [1]. Because of high thermal gradients, metallic structures have traditionally been coated with heat-resistant materials. However, thermal cycling and shock often resulted in cracking and spalling of the coating. Material gradation offered a way of eliminating the deleterious effects of sharp interface. This concept was broadened to include a combination of dissimilar materials without explicit boundaries for creation of materials with new functions. Over the past years FGMs have received increasing interest on a worldwide scale. Today FGMs are used in many diverse areas and some examples include functionally graded bioactive coatings of hydroxyapatite/ titanium oxide [2], graded polymer composites reinforced with ceramic particles [3], Ti-Al$_2$O$_3$ artificial tooth roots [4], and reusable high-performance engines [5].

One of the potential application areas of FGMs is the armor structures composed of layered material systems [6]. Typical layered armor consists of a hard frontal surface layer and a softer backing plate (Figures 1.2(a) and (b)). The layers are usually made of fiber reinforced polymer composites, ceramics, and metals. One of the earliest composite targets investigated by Wilkins [7] was made by simply bonding a ceramic tile to a backing metal plate. Recent armor systems however uses a polymer composite as the backing layer and additional layers such as spall shield and rubber layer between facing layer and backing plate are also included in order to satisfy certain functions.

The underlying idea of layered armor structures is to use a hard ceramic layer to defeat the projectile by inducing a destructive shock wave on to the projectile, and to use a tough backing plate to absorb the impact energy and to act as a catcher for residual broken fragments in preventing target penetration. In this armor scheme, best ballistic protection will be provided by the hardest frontal material used. However, a harder material is also typically brittle and thus exhibits a larger collateral damage area with dynamic impact. This limits the multi-hit capability of such an armor material.
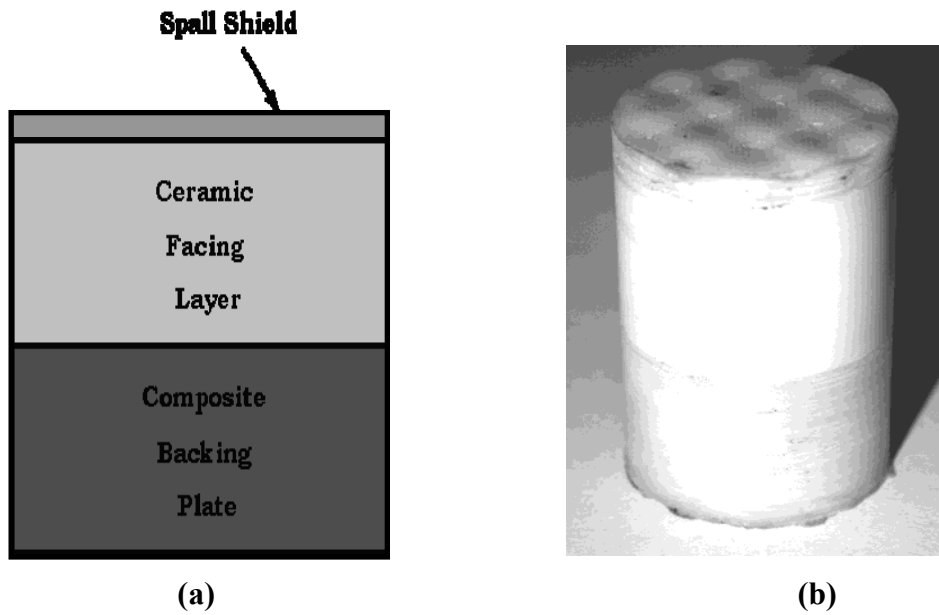
Figure 1.2 Layered armor material system composing of a ceramic facing layer and a polymer composite backing layer (a) schematic and (b) cut-cross-section photograph.

A potential armor material that is being considered by U.S. army is the functionally graded particulate reinforced Al Metal Matrix Composites (MMCs) named as functionally graded armor composites (FGAC) [6]. The idea behind FGAC is to disrupt the shock wave in order to minimize collateral damage during a ballistic event. The hypothesis is to tailor perturbations through microstructural design that prolongs projectile through target dwell time. Thus promoting breakup of the projectile before complete penetration or unacceptable collateral damage of the armor. Resulting in an increased multi-hit capability of the armor.

In this study, FGM systems composing of SiC-particulate Al composites of varying reinforcement volume fractions were investigated for the high strain rate behavior. The results shown in this study were preliminary and forming a basis for future studies of wave propagation effects through the NSF/TUBİTAK project called Wave Propagation in Multi Layer Materials. The material systems studied were prepared in house using a powder metallurgical process. One material system was also modeled using LSDYNA 3 in order to validate the experimental result accuracy and also to develop modeling strategies for future studies.

CHAPTER 3

BACKGROUND

Processing techniques of functionally graded materials are first reviewed and then, modeling approaches for FGMs with emphasis given on the high strain rate applications are discussed in this chapter.

3.1 Processing Techniques for FGMs

Processing techniques for FGMs can be divided into two main groups, namely; powder metallurgy and melt processing. An overview of processing techniques is tabulated in Table 2.1 and in the following sections these techniques are explained in detail. Special emphasis will be given to the powder metallurgy techniques.

Table 2.1 Overview of processing techniques for FGMs [15]

Process	Variability of transition function	Layer thickness	Versatility in phase content	Type of FGM	Versatility in component geometry
Powder stacking	Very good	M, L	Very good	Bulk	Moderate
Sheet lamination	Very good	T, M[b]	Very good	Bulk	Moderate
Wet powder spraying	Very good	UT, T[b]	Very good	Bulk[c]	Moderate
Slurry dipping	Very good	UT, T[b]	Very good	Coating	Good
Jet solidification	Very good	M, L	Very good	Bulk	Very good
Sedimentation/centrifuging	Good	C	Very good	Bulk	Poor
Filtration/slip casting	Very good	C	Very good	Bulk[c]	Good
Laser cladding	Very good	M	Very good	Bulk, coating	Very good
Thermal spraying	Very good	T	Very good	Coating, bulk	Good
Diffusion	Moderate	C	Very good	Joint, coating	Good
Directed solidification	Moderate	C	Moderate	Bulk	Poor
Electrochemical gradation	Moderate	C	Good	Bulk	Good
Foaming of polymers	Moderate	C	Good	Bulk[c]	Good
PVD, CVD	Very good	C	Very good	Coating	Moderate
GMFC process	Very good	M, L, C	Moderate	Bulk	Good

[a] L: large (>1 mm); M: Medium (100-1000 μm); T:thin (10-100 μm); UT: very thin (<10 μm); C: continuous

[b] Depending on available powder size

[c] Maximum thickness is limited

3.1.1 Powder Metallurgy Techniques

The powder metallurgy route offers some advantages especially for the manufacturing of MMCs compared with other techniques like ingot metallurgy and diffusion welding [1, 8]. The low manufacturing temperatures involved in powder metallurgy avoids strong interfacial reactions and minimizes the undesired reactions between the matrix and reinforcement. The uniformity in the reinforcement distribution obtained in this process also improves the structural properties and reproducibility.

The powder metallurgy route includes powder production, powder processing, forming operations, sintering or hot consolidation. Flow chart for powder metallurgical fabrication of functionally graded materials is shown in Figure 2.1 and composed of two different routes; continuous or stepwise FGM preparation.

Continuous or stepwise changing of the gradients in the powder metallurgy processed FGMs could be achieved according to the processing technique used. In the following sections techniques for deposition of powders with stepwise and continuous changes in the mixture are summarized.

```
                    ┌─────────────────────┐
                    │  Starting material  │
                    │ ( metal and ceramic │
                    │  powder & whiskers) │
                    └─────────────────────┘
                              │
                          ┌───────┐
                          │ Mixin │
                          └───────┘
                         /         \
          ┌──────────────┐         ┌──────────────┐
          │  Continuous  │         │   Stepwise   │
          │ Compositional│         │ Compositional│
          └──────────────┘         └──────────────┘
                 │                         │
          ┌──────────────┐         ┌──────────────┐
          │  Suspensio   │         │   Stepwise   │
          │     n        │         │   stacking   │
          └──────────────┘         └──────────────┘
                 │                         │
          ┌──────────────┐         ┌──────────────┐
          │ Spray forming│         │  Precompacti │
          │  on a green  │         └──────────────┘
          └──────────────┘
                    \             /
                    ┌─────────────┐
                    │     CIP     │
                    └─────────────┘
                   /       │       \
        ┌──────────────┐ ┌─────┐ ┌───────┐
        │ Pressureless │ │ Hot │ │  HIP  │
        │  sintering   │ └─────┘ └───────┘
        └──────────────┘    │
                    \       │       /
                    ┌─────────────┐
                    │   (Defect   │
                    └─────────────┘
```
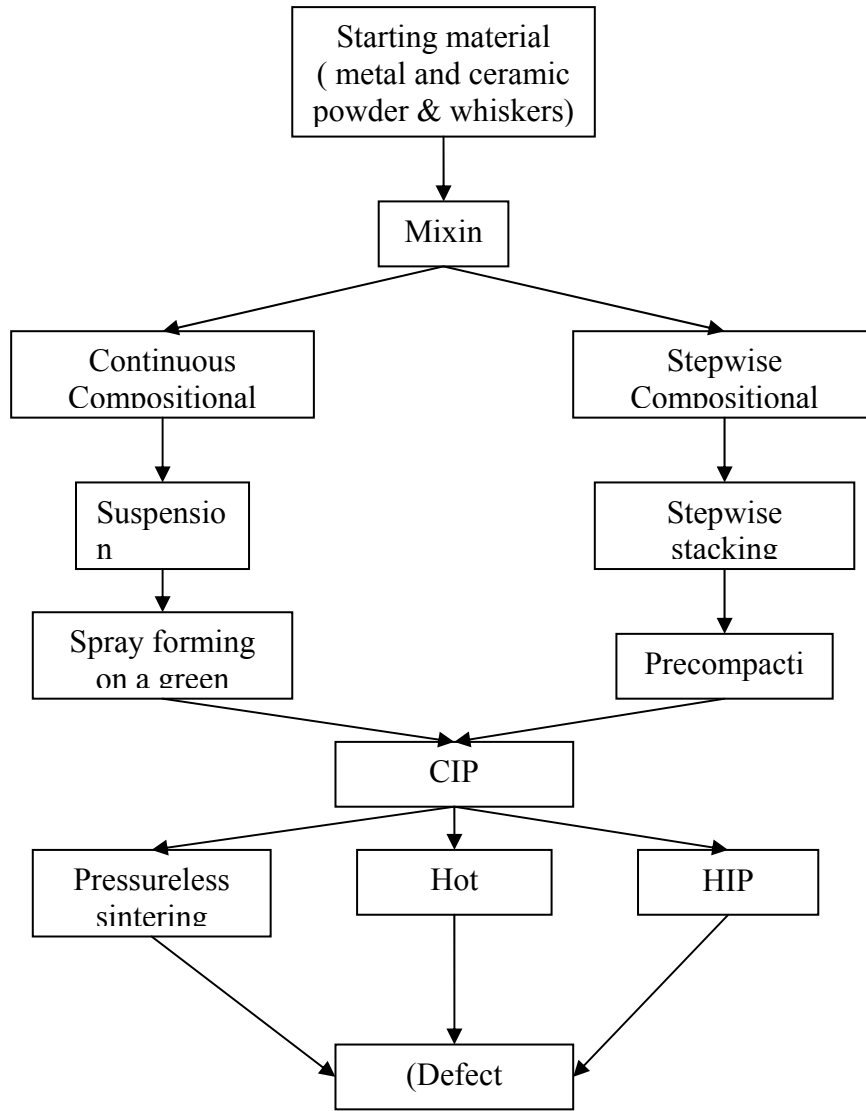
Figure 2.1 Flow chart of powder metallurgical fabrication of FGMs [8].

3.1.1.1   Stepwise Compositional Control

3.1.1.1.1   Powder Stacking (die compaction of layers)

Stepwise gradients can be formed by the deposition of powder layers with changing composition in a compaction die [1, 8]. The disadvantages are the limited thickness and number of layers, discrete changes in the composition, limited size of the part due to limits of compaction powders, discontinuous manufacturing with low productivity. For laboratory studies, the powder stacking method however one of the most convenient way of producing layered structures for requiring simple processing steps and devices. In this thesis the powder stacking method was selected to prepare MMC FGM samples for testing at high strain rates and the details of the processing route are given in Section 3.2.

3.1.1.1.2   Sheet Lamination

Thin sheets of different compositions can be produced by dry or wet powder techniques such as powder rolling or tape casting [9, 10]. These sheets can be joined to form a stepwise gradient. Powder rolling gives green sheets with a thickness in the range of 1 mm. Tape casting of very fine powders allows a sheet thickness in the double digit micrometer range. The number of sheets in the FGM would be limited mainly by the costs of fabrication. Hot pressing is used to join the layers during the final consolidation. This step can be accompanied by a simultaneous combustion synthesis [11].

3.1.1.1.3   Wet Powder Spraying

By including a mixing system and controlled feeding of two or more suspensions graded powder layers can be deposited on a flat, curved or rotating substrate. Coatings of different materials with controlled variety of porosity and thickness were produced by applying powder suspensions on a substrate by means of an air or manual brush [12].

3.1.1.1.4   Solid Freeform Processes

Solid Freeform Fabrication (SFF) refers to a class of manufacturing processes that build objects in an additive fashion directly from a computer model. While some SFF processes are restricted to building in a single material at a time, most can be adapted to have some degree of control over the local composition [13]. An approach to modeling a part's geometry, topology, and composition based on subdividing the solid model into sub-regions and associating analytical composition blending functions with each region, in order to provide control on local composition using SFF processes was discussed by Jackson *et. al.* [14].

3.1.1.2   Continuous Composition Control

3.1.1.2.1   Centrifugal Powder Forming (CPF) and Impeller Dry Blending

In CPF, powder mixtures with computer controlled continuous change of composition are fed onto a rotating distributor plate, which accelerates towards the inner wall of a rotating cylinder. A green body of sufficient strength is formed by simultaneously spraying an organic binder onto the wall. The method is limited to cylindrical parts but offers a great flexibility in gradient design.

Centrifugal powder forming in combination with liquid phase sintering was used in German priority program on FGMs for the production of W/Cu FGMs [15].

The impeller-dry-blending process for manufacturing of FGM parts involves four stages, through which the powders pass, in sequence,

   i.   Feeding of the two component powders from two separate feed-hoppers.
  ii.   Blending of powders by metering of the ratios of the two powder streams using control gates.
 iii.   Homogenisation of the blended powder mix using an impeller chamber.
 iv.   Deposition: the homogenised blend deposits like into a mold beneath the impeller chamber.

Ruys *et. al.* [16] have investigated the silicon carbide-stainless steel and the silicon carbide–copper FGM systems using impeller-dry-blending process.

3.1.1.2.2 Centrifugal Sedimentation

The formation of tubular structures with a continuous particle gradient is possible if a hollow cylindrical mold is filled with a suspension of dispersed powder with a size distribution centrifuged around its center axis [17]. Due to the limited concentration in the suspension only thin layers can be produced. Pore-size graded ceramic filters were made by centrifugal deposition of TiO_2 powders from aqueous suspensions [15].

3.1.1.2.3 Electrophoretic Deposition

Electrophoretic deposition from suspensions containing more than one component can be used to produce graded bodies. In the simplest case an external mixing system supplies suspensions with the variable concentrations of the components or the second component is added with time in calculated proportions. Functionally graded WC–Co materials were fabricated using electrophoretic deposition from a suspension of hard metal powder in acetone, with variable cobalt content. The deposits were sintered to closed porosity at 1290 and 1340 °C [18].

3.1.1.2.4 Pressure Filtration/ Vacuum Slip Casting

By continuously changing the powder composition supplied to the filtration system, a defined one-dimensional gradient in the deposit it is obtained. The same principles can be applied to slip casting. Sequential slip casting is proposed as an alternative route for the future family of dense functionally gradient ceramics (FGCs) with complex shapes and tailored microarchitectures [19]. Following this route an alumina/yttria tetragonal zircona polycrystal (Y-TZP) FGC with close to theoretical density, homogeneous layers and sharp layer interfaces has been obtained [19].

3.1.2   Melting Processes

Gradient formation can be achieved by transport processes in the molten state and subsequent consolidation.

3.1.2.1   Centrifugal Casting

In centrifugal casting, particles of a refractory phase are dispersed in a metal melt. These particles may be formed in situ during cooling of the melt or dispersed in a preceding step. The density difference between particles and the melt leads to the particle concentration gradient if the melt is cast in a centrifuge. Using centrifugal casting method Zhang *et. al.* [20] produced functionally graded Al/Mg_2Si tubes with reinforcements in both the inside and outside walls of the tubes [20]. Another example is $Al-Al_3Ti$ functionally graded materials (FGMs) fabricated by using centrifugal casting technique [21].

In order to study the formation process of composition gradient, the motion of ceramic particles in a molten metal of a viscous liquid under a centrifugal force was numerically modelled by Watanabe *et. al.* [22]. Experiments that used a plaster-corundum model FGM were simulated using the model. It was concluded that greater gradients were obtained in case of thinner thicknesses, greater centrifugal forces and smaller mesh size particles. The processing of mixed particle sizes was also examined and it was found to be useful to control the composition of metal-ceramic FGMs manufactured by the centrifugal method.

3.1.2.2   Sedimentation Casting

With wet molding, it is possible to control the sedimentation velocities of particles in slurry by verifying the viscosities of dispersion media used in the molding process. Arata *et. al.* [23] adopted uniaxial wet-molding to fabricate continuously graded $WSi_2 - ZrO_2$ (2Y) materials.

3.1.2.3 Infiltration Processing

Infiltration is a suitable processing method for FGMs containing phases of very different melting points. In this process a preform of the more refractory phase possessing a porosity gradient is produced and infiltrated with the melt of the lower melting component at elevated temperatures. This method is particularly attractive for metal-ceramic FGMs [24, 25, 26].

There are various processing approaches like, using a volatile component, using ceramic powder layers with different strain rates, using composition dependent reactive sintering, for creating porosity gradient ceramic preforms [24].

Fabrication of functionally graded Al–Mg/ZrO$_2$ components was studied by Corbin *et. al.* [25] and magnesium alloyed Al, spontaneously infiltrated through ZrO$_2$ preforms with a graded porous structure under N$_2$ atmosphere and functionally graded Al–Mg/ZrO$_2$ components were prepared. Infiltration-processed, functionally graded aluminium titanate/ zirconia-alumina composites were also studied [26].

3.1.2.4 Thermal Spray Processing of FGMs

In thermal spraying, the feedstock material (in the form of powder, rod or wire) is introduced into a combustion or plasma flame. The particles in melt transit and impinge on the substrate where they rapidly solidify and form a deposit. According to the type of the heat source and the method of injection of the feedstock thermal spray techniques can be classified as arc spray, combustion and plasma spray [27]. Electrically conductive wires are used as feedstock in arc spray processes. Feedstock in the form of powder or wire is used in combustion processing and plasma spraying uses feedstock in the form of powder.

In plasma spray several approaches can be used to form graded structures. One of them is using multiple torches with independent feeding systems for each component to independently deposit metal and ceramic layers [27]. Schematic of a typical dc plasma-spray torch is given in Figure 2.2 and schematic illustration of the use of multiple torches is shown in Figure 2.3.
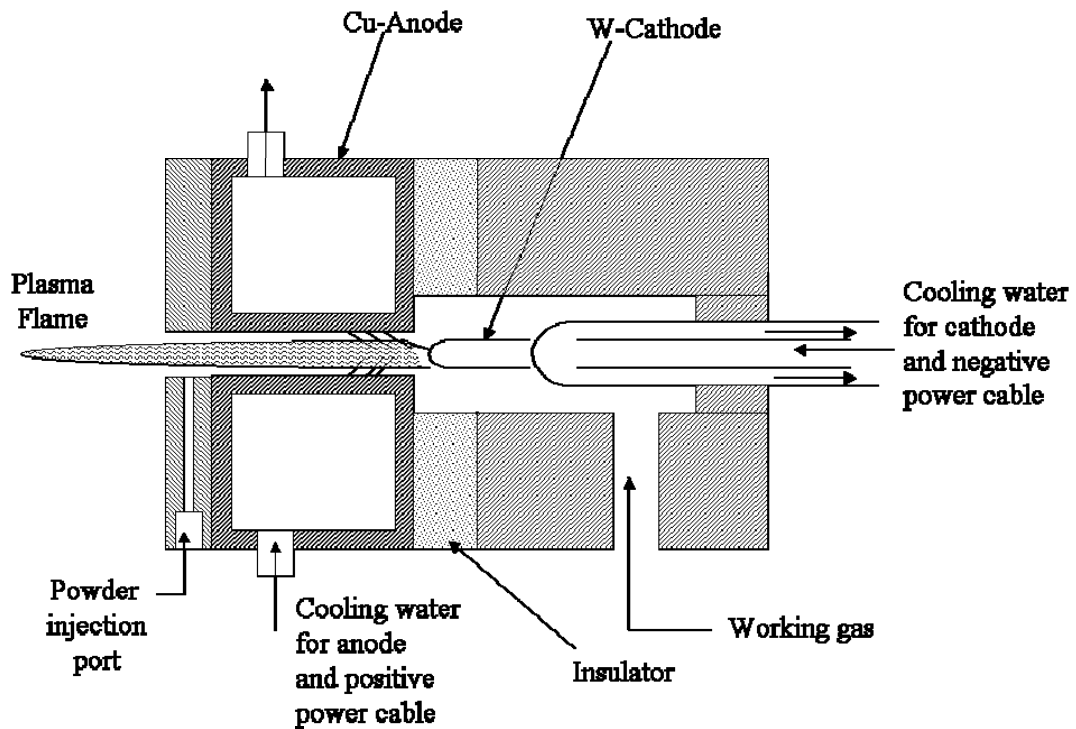
Figure 2.2 Schematic of a typical dc plasma-spray torch [27].
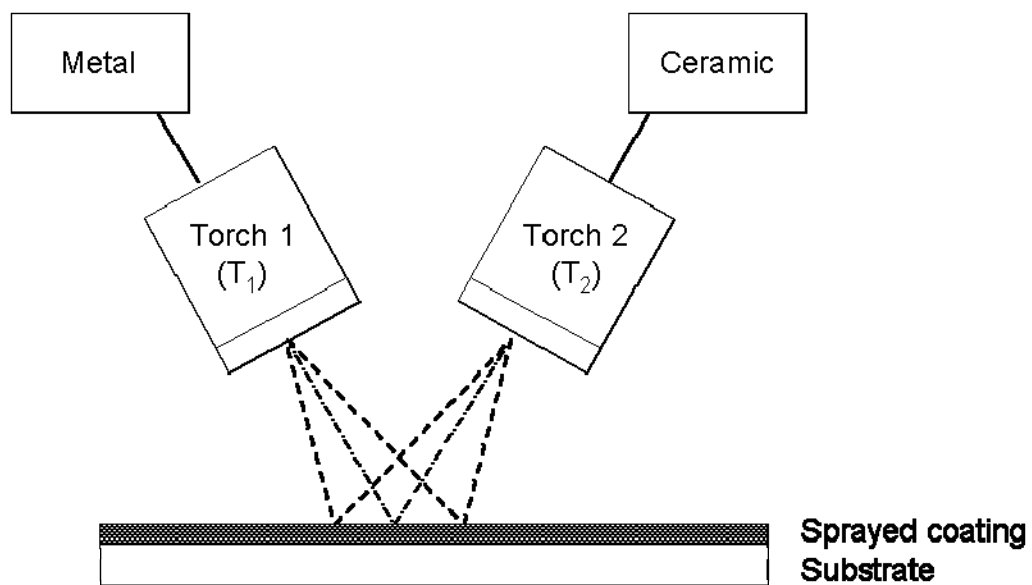
Figure 2.3 Schematic illustration of the use of multiple torches [27].

Plasma sprayed FGMs of NiCrAlY- (ZrO_2-Y_2O_3), Ni-Al_2O_3 and NiCr-8PSZ were discussed in [27] in detail.

3.2   Modelling of FGMs

In designing functionally graded materials with optimum composition profile for the desired function, the detailed data of the dependencies of thermal and mechanical properties on compositional and microstructural variations are necessary. In the simplest case, the structure of a material is represented by the model-like system of a matrix with embedded particles. For such composites, the microstructural fields could be assumed to be homogeneous. On the other hand, the traditional approximations and models are not directly applicable to FGMs because of the gradients in functionally graded materials. Most of the models used for FGMs are based on the Finite Element Method (FEM) and its variations. Many of the models however concern the performance of FGMs under thermal loading [28-31].

In order to understand and optimize the materials for the dynamic failure events occurring in high strain rate loading, stress wave propagation analysis especially in FGMs is required. For an impact event many different kinds of waves are initially generated and propagate [32]. Common types of elastic waves in solids are;

   i. longitudinal (dilatational or irrotational) waves,

   ii. distortional (shear, or transverse, or equivolumal) waves,

   iii. surface (Rayleigh) waves,

   iv. interfacial (Stoneley) waves,

   v. bending (flexural) waves (in bars and plates).

Among these waves, the compressive longitudinal waves usually contain most of the energy [32]. During wave propagation in a typical energy absorbing system consisting of dissimilar materials, impacted material is harder or having higher mechanical impedance than the backing plate [7,33-37]. Thus the initial compressive wave formed on the facing layer reflects back as a tensile wave from the facing layer-backing plate interface leading to localized failure. Using however tailored graded interfaces instead of sharp interfaces between dissimilar materials could attenuate the reflection of stress waves and delay the failure of individual components and delocalise the failure of the system [6,38]. Therefore attenuation of reflection of stress waves is an important criterion in designing interfaces of energy absorbing structures.

Bruck developed a 1-D model for designing FGMs to manage stress waves [38]. He considered stress waves as linearly elastic longitudinal waves propagating in one dimension through a discretely layered FGM as depicted in Figure 2.4. At each interface the stress waves are partially reflected and partially transmitted as shown in the same figure. Following results have been pointed out in the model,

i.   The peak stress of waves reflected from the FGM interface was slightly greater than for materials with sharp interfaces.

ii. The benefit of the FGM over the sharp interface was to introduce a time delay to the reflected wave propagation when stresses approached peak level.

iii. The time delay was highly dependent on the composition gradient and the differences in base material properties.

iv. The proposed model could be experimentally verified by testing FGM specimens in a Split Hopkinson Pressure Bar (SHPB).
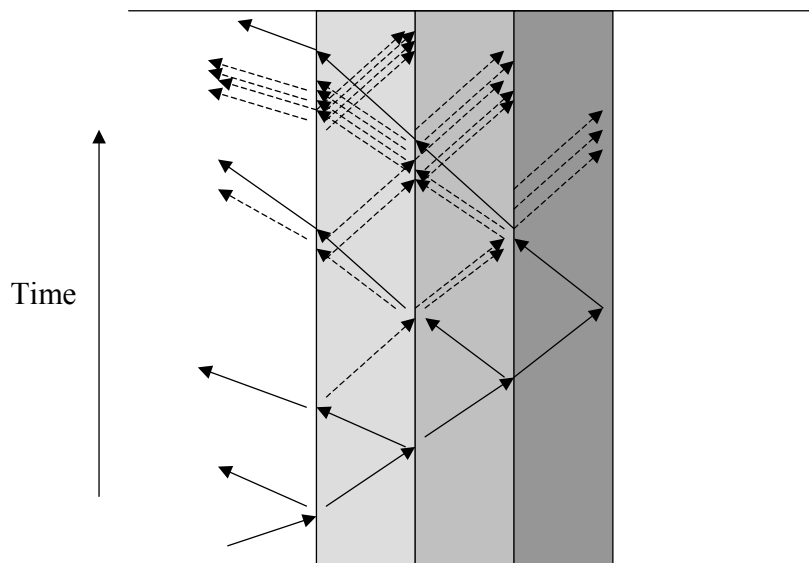
Figure 2.4 One-dimensional stress wave propagation through discretely layered FGM (the waves reflected from multiple interfaces are designated by dashed arrows) [38].

The layered and graded plates of particle reinforced MMCs of varying volume fraction of reinforcement through the thickness were examined by Y. Li *et.al.* [39]. The result of high strain rate tests were used to develop a model for the viscoplastic response of the composite and numerical investigation of the propagation of large

amplitude stress waves were conducted based on the model. The following conclusions were drawn;

    i.   Sharp or discontinuous interfaces have strong value in structural design for dynamic problems.

    ii.   Complex coupling of elastic and viscoplastic responses involved during wave propagation within layered and graded composites.

    iii.   The location and timing of spall failure and the magnitude of the local tensile stresses could be controlled by properly grading or layering the reinforcement volume fraction.

    iv.   Gradation or layering the reinforcement volume fraction was also important in controlling the location, timing and magnitude of maximum plastic strain and the extent of the overall plastic zone.

    v.   Evaluating the performance of impacted structures, by evaluating the dissipated energy and strain energy fractions with time indicated that grading and layering provided additional opportunities for optimizing the performance of structures in impact applications.

Modeling of FGMs in dynamic analyses was further discussed by Banks-Sills *et. al.* [40]. The effects of using different types of finite element approximations on the predicted stress wave propagation through a graded material were investigated. Using conventional elements they simulated one dimensional stress waves using a distinct phase model, a discretely layered model and a smoothly varying model. Results of the simulations showed that different discretization caused a relative shift in the wave speed and the magnitude of this shift increased with time.

The property gradient in a continuously nonhomogeneous material will cause a continuous change in acoustic impedance as a function of position. Using conventional elements in modeling elastic stress wave propagation in a graded material produces a piece-wise constant approximation for the actual impedance and this causes distinct boundaries for the stress waves where in the actual nonhomogeneous system these distinct boundaries do not exist [40]. Thus using graded finite elements in modeling the stress wave propagation in continuously nonhomogeneous materials can be beneficial [41].

Besides numerical approaches micromechanical modeling of FGMs, for property evaluation were investigated by Gasik [42].

CHAPTER 4

MATERIALS AND MMC PROCESSING

4.1   Materials

The specifications of materials, aluminum powder and SiC_p, used to prepare FG-MMCs are listed in Table 3.1. The particle sizes of the Al powder and SiC_p were measured with a Micromeritics Particle Size Analyzer and the results are shown in Figures 3.1 and 3.2. Mean particle sizes were found to be 37 and 22 μm for Al powder and SiC_p, respectively. Aluminum powder with a relatively low impurity content (<1%) was preferred over an alloy powder in order to reduce the extent of reactions between SiC_p and alloying elements.

Table 3.1 Specifications of Al and SiC powders.

Powders	Size (μm)	Purity	Measured mean diameter (μm)	D (10%) (μm)	D (50%) (μm)	D (90%) (μm)
Al powder (Aldrich)	< 74	99%	37.13	17.32	34.64	69.28
SiCp (Aldrich)	< 37		20.12	12.25	22.3	33.4
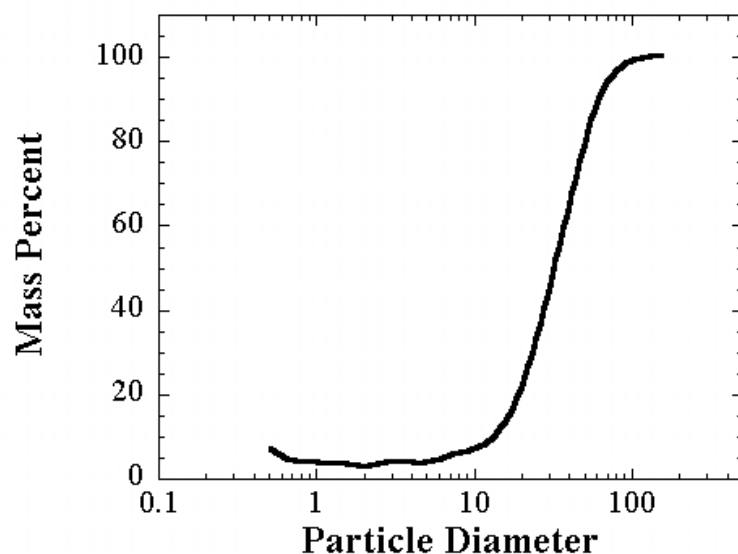
Figure 3.1 Mass Percent vs. Particle Diameter of as-received Al powder.
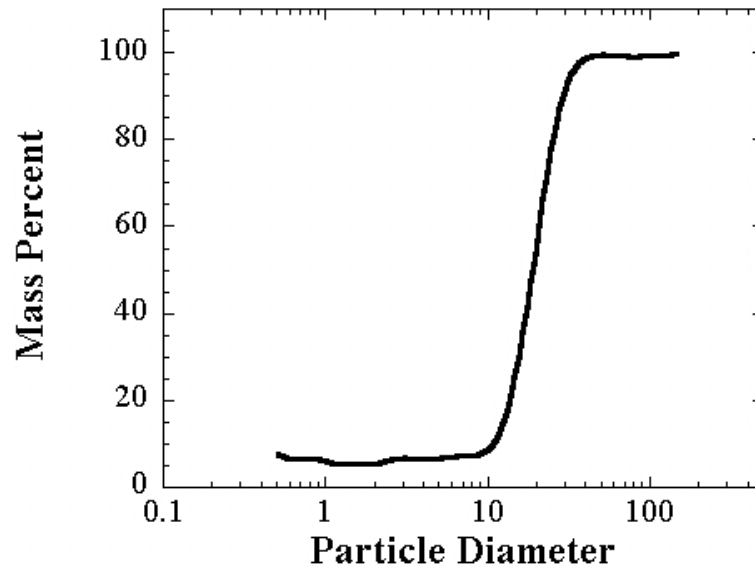
Figure 3.2 Mass Percent vs. Particle Diameter of as-received SiC powder.

4.2 Processing Route

Both single layer and multi-layer composites were prepared using a powder metallurgy route schematically shown in Figure 3.3. The process starts with the mixing of appropriate amounts of basic ingredients (Al and SiC powders) inside a plastic container, which was rotated on a rotary mill in order to form a homogeneous powder mixture. Then powder mixture is compacted at 600 MPa in a cylindrical steel die with a diameter of 16 mm (Figures 3.4 and 3.5) using a uniaxial hydraulic press. For the multi-layer samples thickness of the individual layers is adjusted to be equal. In the compaction of multi-layer samples, the layers are sequentially pre-compressed at a lower stress (100 MPa) and then they were compacted altogether at 600 MPa in order to provide a strong bonding between layers. Resulting samples are cylindrical in shape with 16 mm and 10 mm in diameter and height respectively. In a further step the cold compacts are heat-treated at 650°C for 1 hour in a Protherm PLF160 laboratory furnace in order to homogenize the compacts and relief the stress concentrations. The heat treatment is performed in an enclosed steel box (welded steel box) in order to prevent the oxidation of the compacts. The heat treated MMCs samples are then quasi-statically deformed using a Shimadzu AG-I 250KN Tension-Compression Test Machine at a strain-rate of $1.7x\ 10^{-3}\ s^{-1}$ up to 60% strain. During compression testing the interface

between two layers bends at the edges because of the difference between the Poisons ratios of the layers. Such a bend interface is shown in Figure 3.6 for a 2-layer sample after quasi-static deformation. Finally to obtain a straight interface between layers, the deformed samples are cut into a square cross-section of 10 mm long as shown in Figure 3.6 with dash lines. These samples are further compressed at various strain rates in order to see the effect of strain rate on the deformation behavior. Using above technique, relatively dense single and multi layered MMCs were prepared.

```
┌─────────────────┐
│     Mixing      │
│    Al & SiC     │
│    powders      │
└─────────────────┘
         │
         ▼
┌─────────────────┐
│  Cold Pressing  │
│    (600 MPa)    │
└─────────────────┘
         │
         ▼
┌─────────────────┐
│    Sintering    │
│  (650 °C, 1 hr) │
└─────────────────┘
         │
         ▼
┌─────────────────┐
│   Quasi-static  │
│   deformation   │
│ (up to 60% strain)│
└─────────────────┘
         │
         ▼
┌─────────────────┐
│     Cutting     │
└─────────────────┘
```
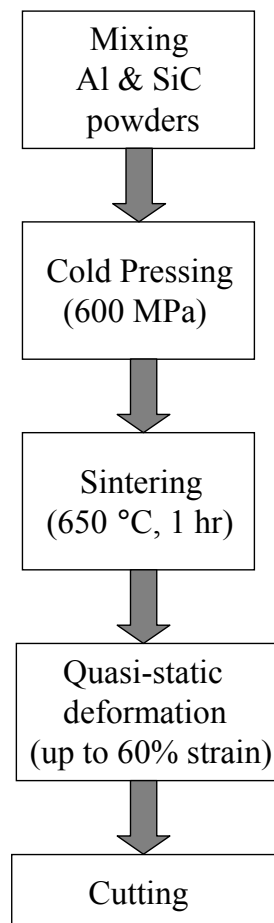
Figure 3.3 Schematics of sample preparation.
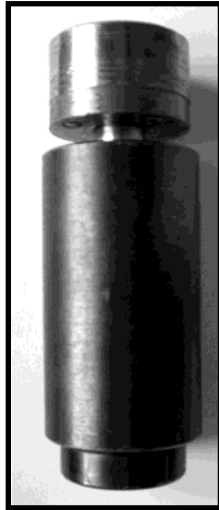
Figure 3.4 Photograph of the steel die.
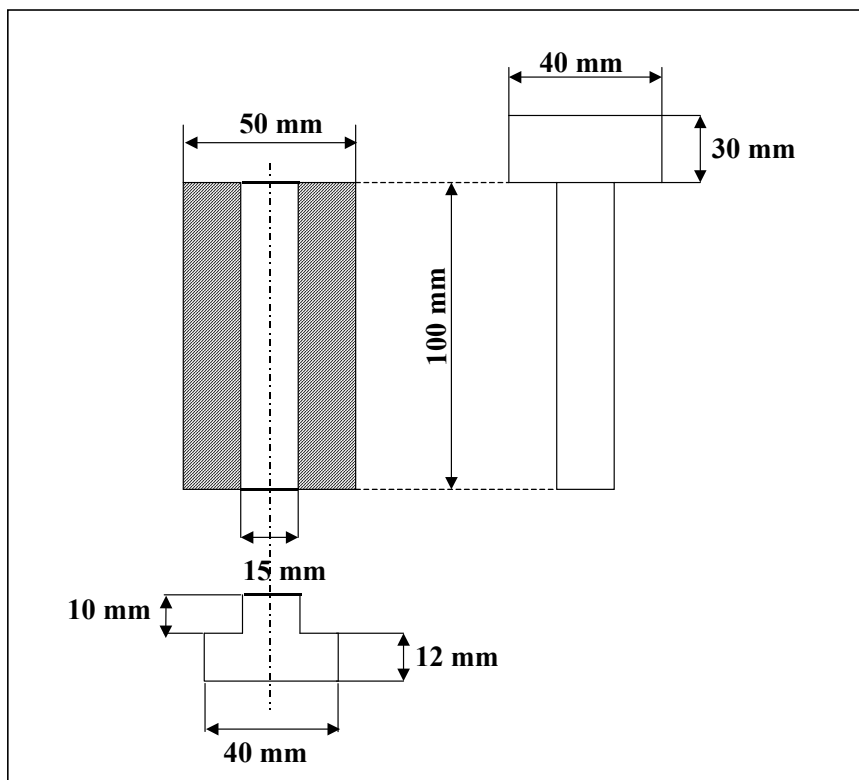
Figure 3.5 Dimensions of the steel die.
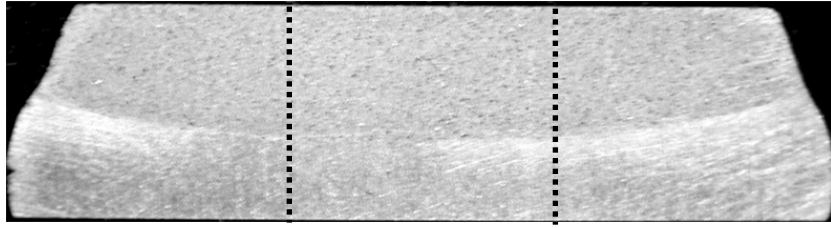
Figure 3.6 Photograph of a 2-layer sample after deformation.

Using the above process, eight different types of single-layer and multi-layer composites were prepared. Schematic representation of the manufactured samples is also shown in Figure 3.7. Three single layer samples includes 0, 10 and 20% SiC_p Al MMCs and others are 2, 3, 5 and 6-layer MMCs.
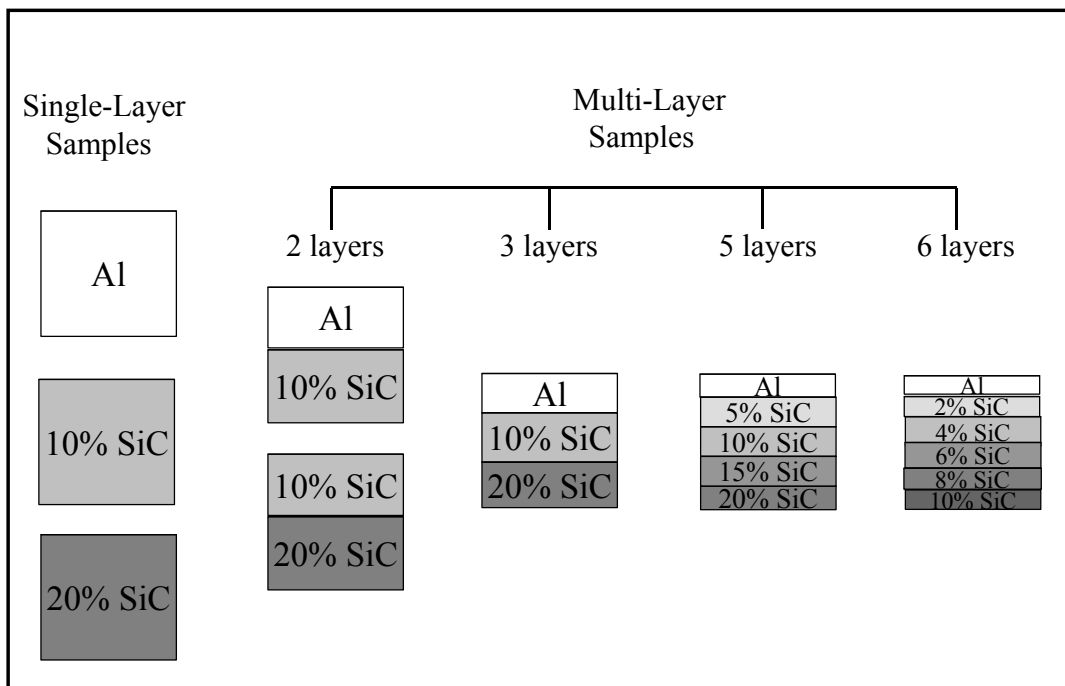
Figure 3.7 Schematic representation of manufactured samples.

In order to provide easiness, single-layer samples are named according to the SiC % and the multi-layer samples are named according to SiC % of the individual layers separated by slashes as tabulated in Table 3.2.

Table 3.2 Naming of manufactured samples.

	SiC% (vol)
Single-Layer Samples	0 (pure Al)
	10
	20
Multi-Layer Samples	0/10
	10/20
	0/10/20
	0/2/4/6/8/10
	0/5/10/15/20

4.3   Density Measurement

The densities of the prepared samples, both before and after quasi-static compression were measured using the Archimedes density measurement kit of Precisa XB 220A balance (Figure 3.8). The method is based on the Archimedes' principle; the apparent weight of an object immersed in a liquid decreases by an amount equal to the weight of the volume of the liquid that it displaces. For density measurement, first the temperature of the water is read using the thermometer immersed in water (Figure 3.8) and then set in the balance. The balance set the density of the water according to the temperature value automatically. After setting the water temperature, the sample is inserted into the upper cup (Figure3.8(a)) and weight value is recorded in the balance. Later, the sample is inserted into the lower cup, which is in water (Figure3.8(b)). Again the weight value is recorded in the balance. Following Archimedes' principle, the difference between two recorded values is equal to the weight of the water displaced by the sample. The balance automatically calculates the density of the sample using the recorded data.
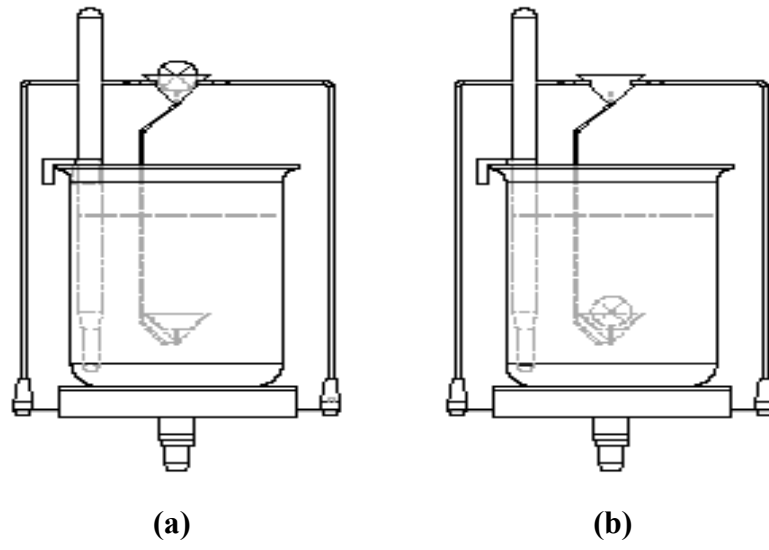
(a)   **(b)**

Figure 3.8 Schematics of density measurement kit.

CHAPTER 5

TESTING METHODS AND MODELING

Two different types of compression tests were carried out, namely, quasi-static and high strain rate. Quasi-static tests were performed using a Shimadzu AG-I 250KN Tension-Compression Test Machine at a cross-head speed of 1 mm min^{-1} corresponding a strain rate of 1.7x 10^{-3} s^{-1}. High strain rate tests were conducted with a compression type Split Hopkinson Pressure Bar (SHPB) at University of Delaware within the strain rate range between 1000 s^{-1} and 3500 s^{-1}. These two techniques were, therefore, used to obtain quasi-static and high strain rate stress-strain curves of the both single layer and graded Al/SiC$_p$ composites.

5.1 Quasi-Static Testing

It is well known that all testing machines and auxiliary apparatus deflect under the load during any test. Therefore, the displacement during compression testing is the sum of the machine (δ_m) and specimen (δ) displacements. If v_{CR} is the cross-head speed of the testing machine and t is the time, the total displacement may be written as

$$\delta_t = \delta + \delta_m = v_{CR}t = e\,l\,+\frac{F}{K} \tag{4.1}$$

where e, l, F and K are the engineering strain, initial length of the specimen, instantaneous load and machine stiffness, respectively. The second term of Equation (4.1) represents the machine displacement at an instantaneous load. By arranging Equation (4.1), specimen strain is written as

$$e = \frac{(v_{CR}t - \frac{F}{K})}{l} \tag{4.2}$$

The value of K was calculated by compression the test plates up to the maximum load that was reached during the tests of the specimen. Engineering stress (S), true stresses(σ) and true strain(ε) were calculated using the equations (4.3), (4.4) and (4.5) respectively:

$$S = \frac{F}{A_0} \qquad\qquad (4.3)$$

where A_0 is the initial cross-sectional area of the sample,

$$\sigma = S(1 - e) \qquad\qquad (4.4)$$

$$\varepsilon = \ln(1 - e) \qquad\qquad (4.5)$$

5.2   High Strain Rate Testing

5.2.1   Historical Development of SHPB

As the nineteenth century progressed, there was an increasing awareness that the properties of materials under impact differed from those under static loading. Historically, the first experimental study of high strain rate deformation was reported by J. Hopkinson in 1872 [43], he used a long thin bar known as the Hopkinson Pressure Bar, to measure the pulse shape induced by an impact. In 1948, Davies developed a technique using condensers to measure the strains existing in the pressure bar. The following year Kolsky added a second pressure bar to Hopkinson's original apparatus, hence the name *Split* Hopkinson bar. In 1970, Hauser *et al.* added strain gauges to the Split Hopkinson bar to measure surface displacements. The split Hopkinson bar technique, which has been initially used in compression, has been extended to tension [44] and torsion [45]. An arrangement, which permits, loading with one and just one pulse in compression, as well as in tension, has been reported in the work of Nemat-Nasser and co-workers [46].

5.2.2 SHPB Apparatus

The Split Hopkinson Pressure Bar at University of Delaware consists of a gas gun assembly, three bars and an electronic data measuring system as shown in Figure 4.1. Striker bar, incident bar and transmitter bar are all 19 mm in diameter and made of Inconel 718 due to its high yield strength of 1036 MPa. The incident and transmitter bars have lengths of 3658 mm and 1440 mm.
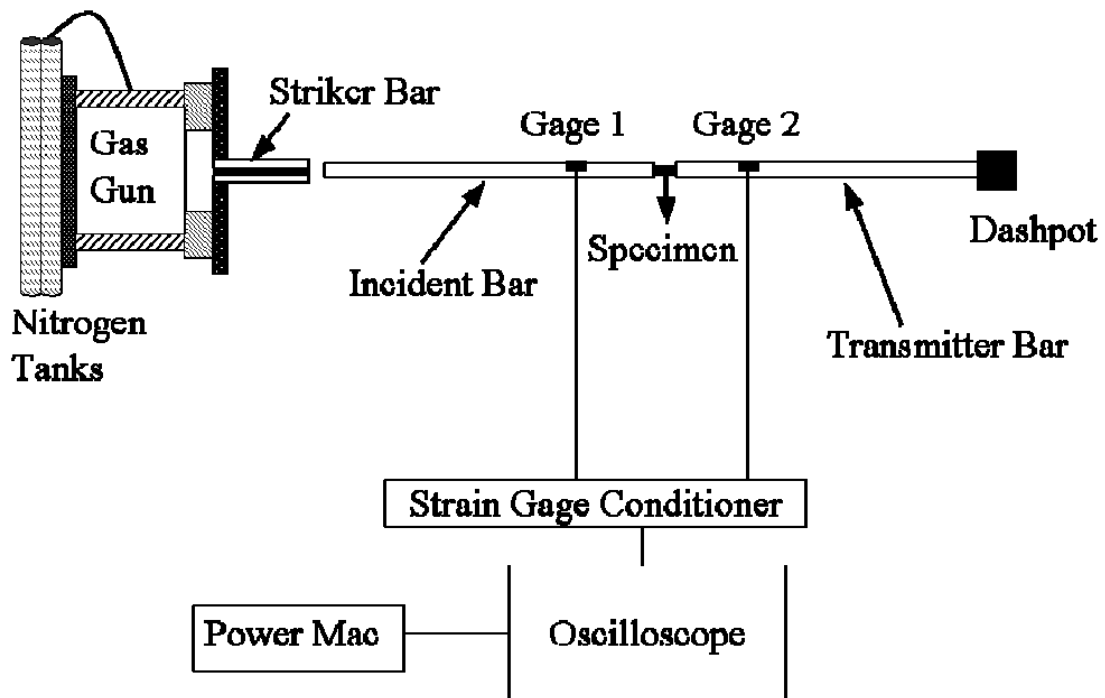

Figure 4.1 Schematic representation of SHPB at University of Delaware.

The gas gun assembly consists of an inner chamber, an outer chamber, and an inner piston as shown Figure 4.2. Initially, the pressurized nitrogen gas in the inner chamber is released to push the piston against the outlet, and then the nitrogen gas is released to fill the outer chamber with a smaller pressure value, which makes a positive difference between inner chamber and outer chamber to seal the outlet. When fired, the nitrogen gas in the inner chamber escapes through the hole, the piston moving to left and the pressurized nitrogen gas in the outer chamber is emptied into the barrel, moving the striker bar horizontally until it hits the incident bar end. The striker bar velocity and subsequently the strain rate are proportional to the outer chamber pressure. Thus the velocity of the striker bar is measured just before impact of the striker bar on to the

incident bar by the help of two infrared beams and a timer connected to the infrared beam system, in each test.
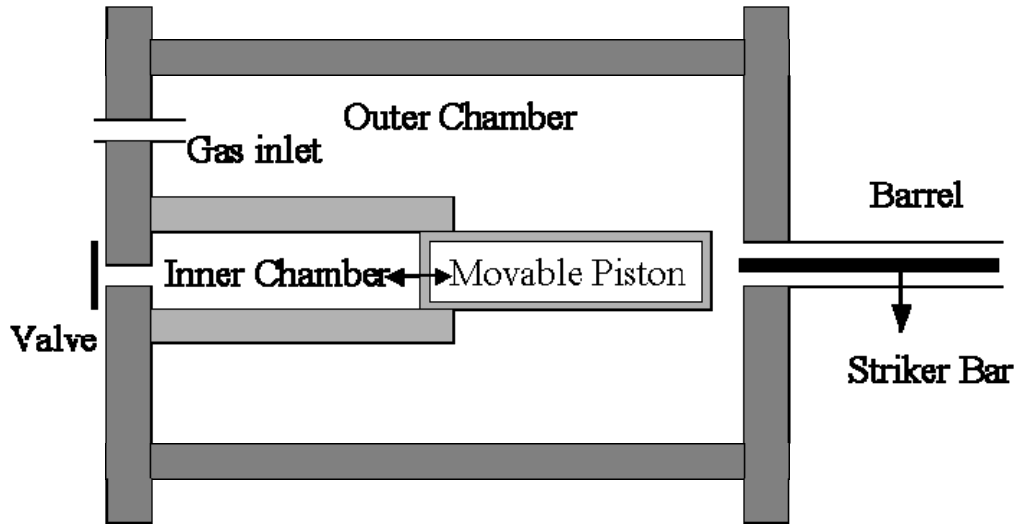

Figure 4.2 Schematic Representation of Gas Gun.

Upon impact, a compressive stress wave is generated and travels down along the incident bar towards the specimen. When it arrives at the interface between incident bar and the specimen, the wave partially reflects back as a tensile wave and the remainder transmits through the specimen into the transmitter bar. The relative magnitudes of the reflected and transmitted waves are a function of the difference in acoustic impedance of the specimen and the bar materials. At the interface of the specimen and the transmitter bar, part of the wave again reflects into the specimen. The dashpot is to protect the bar end from damage during the test.

The electronic measuring system consists of the strain gage conditioner and the oscilloscope connected to a computer. Two strain gauges are used to measure strains on the incident and transmitter bars. Gage 1 on the incident bar measures both incident and reflected pulses while Gage 2 on the transmitter bar measures only transmitted pulse. Both Gage 1 and Gage 2 are connected to a Vishay 2120 strain gage conditioner. Strain gage voltages are recorded and displayed on a Fluke PM3394A oscilloscope connected to the strain gage conditioner. Finally, the data are downloaded to a computer where data reduction is conducted using a software named KaleidaGraph 3.5. Typical SHPB data of incident, reflected and transmitted strain readings are shown in Figure 4.3.

One of the problems of SHPB testing is that samples may remain between the bars and be further deformed by subsequent compression waves reflected back from the incident bar end where striker bar impacts. However, since in the present SHPB the transmitter bar is shorter than the incident bar, before the reflected wave reaches the specimen after reflection from incident bar end as compression wave, the transmitter wave reflects as tensile wave from the end of the transmitter bar and separates the specimen from the bars.
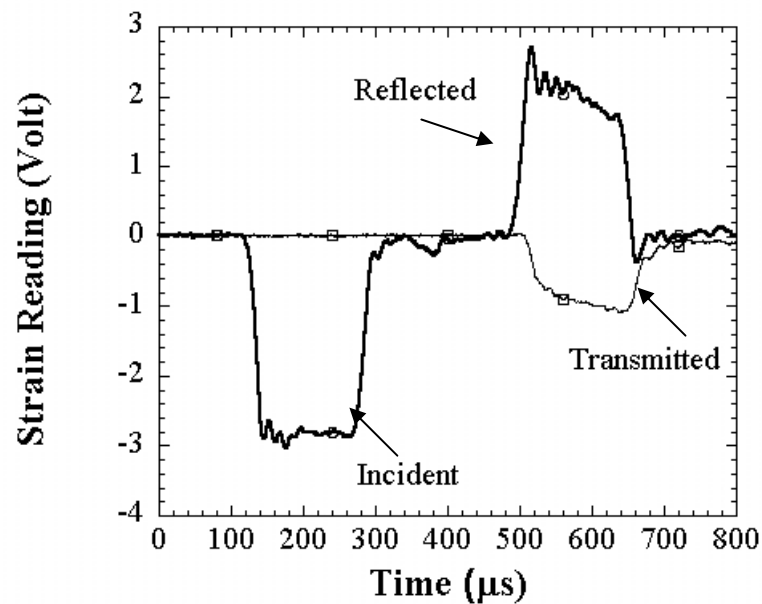

Figure 4.3 Typical SHPB data.

5.2.3   SHPB Analysis

SHPB principles are based on uniaxial elastic wave propagation in long bars. When a long bar having a velocity of v_O strikes another long bar at rest and having the same elastic modulus and diameter as the impact bar, a rectangular elastic stress pulse is produced in the impacted bar and the magnitude of stress and strain are direct functions of the velocity of the striking bar, modulus (E) and elastic wave velocity (C) of the impacted bar. The maximum stress (σ) and the maximum strain (ε) in the bar are given as follows [47]

$$\sigma_b = \frac{v_o E_b}{2C_b} \tag{4.6}$$

27

and

$$\varepsilon_b = \frac{v_o}{2C_b} \tag{4.7}$$

where b refers to the bar. The wave velocity is calculated from the elastic wave theory as

$$C_b = \sqrt{\frac{E_b}{\rho}} \tag{4.8}$$

where ρ is density of the bar.

The displacements of the incident and transmitter bars, u_1 and u_2 can be found using the following equations.

$$u_1 = C_b \int_0^t (-\varepsilon_i + \varepsilon_r)d\tau \tag{4.9}$$

and

$$u_2 = -C_b \int_0^t \varepsilon_t d\tau \tag{4.10}$$

where i, r and t refer to incident, reflected and transmitted waves, respectively. The strain in the specimen is then

$$\varepsilon_s = \frac{u_2 - u_1}{L_s} = \frac{C_o}{L_s} \int_0^t (-\varepsilon_t + \varepsilon_i - \varepsilon_r)d\tau \tag{4.11}$$

where L is the length and s refers to the specimen. The loads on each interface, incident bar/specimen (1) and specimen/transmitter bar (2), are

$$P_1 = A_b E_b (\varepsilon_i + \varepsilon_r) \tag{4.12}$$

and

$$P_2 = A_b E_b \varepsilon_t \tag{4.13}$$

28

A is the cross-section. It is assumed that the wave propagation effect in the small sample may be neglected, so that $P_1 = P_2$. Therefore, Equation (4.11) can be written as

$$\varepsilon_s = \frac{-2C_b}{L_s} \int_0^t \varepsilon_r d\tau \tag{4.14}$$

Accordingly, the stress in the specimen is

$$\sigma_s = \frac{P_1}{A_s} = \frac{P_2}{A_s} = \frac{A_b}{A_s} E_b \varepsilon_t \tag{4.15}$$

5.2.4 SHPB Data Reduction

In order to calculate strain, strain rate and stress, the specimen length and cross sectional area were measured before each test. Data reduction process was applied, after obtaining strain measurements from incident and transmitter bars. The strain in the specimen was calculated using the relation

$$\varepsilon_S = -\frac{2C_b}{L_s} \left(\frac{2\int \varepsilon_r (V) dt}{G_g K_g V_e (1+\varphi)} \right) \tag{4.16}$$

where G_g, K_g, V_e and φ are the strain gage conditioner gain, strain gage factor, excitation voltage of the strain gage bridge and Poisson's ratio of the bar material, respectively. Similarly the stress in the specimen was calculated using,

$$\sigma_S = \frac{A_b}{A_s} E_b \left(\frac{2\varepsilon_t (V)}{G_g K_g V_e (1+\varphi)} \right) \tag{4.17}$$

where the values of C_b, E_b, G_g, K_g, V_e and φ are 4930 m/s, 200 GPa, 200, 2.09, 9.75 V and 0.29 respectively.

5.3 Modeling

A three-dimensional SHPB finite element model has been used to study the stress wave propagation in 10/20 multi-layer MMCs. The results were compared with those of experiments. The analyses were performed using a commercial explicit finite element code LS-DYNA 960 at University of Delaware. Two axes of symmetry were assumed so only one quarter of the bar was modeled. For the test modeled, the output was displayed at several locations within the sample as well as at the location of the strain gages on the incident and transmitter bars of the SHPB apparatus. The desired ideal result is, thus, that the output calculated from the model exactly matches the data measured by the strain gages on the incident and transmitter bars since this would indicate that the model is accurately capturing the wave propagation behavior in the sample and bars.

The model has four components in contact; a striker bar of length 356 mm, an incident bar and a transmission bar each of length 1524 mm, and the specimen, the MMC composite layers with thickness of 2.5 mm. The bar diameter is 19.05 mm and the length of the square specimen is 5 mm. The component materials are modeled with eight nodes solid elements and the interfaces are modeled with the automatic contact sliding interfaces without friction. The impact velocity of the striker bar (V=16.0 m/s) has been defined as the initial condition and all other boundaries are traction free and can move in any direction. In order to save computation time, the simulation uses bars 1524 mm in length instead of full-length bars.

Material properties used in the finite element code are determined experimentally for each layer and the Inconel bars have been modeled with an isotropic elastic material model.

CHAPTER 6

RESULTS AND DISCUSSIONS

6.1   Density Measurements

Densities of both single-layer and multi-layer samples were measured and relative densities were calculated as explained in section 3.3, before and after quasi-static deformation. The density measurement results are shown in Figure 5.1 for single and multiple layer samples. Also as shown in this figure, the quasi-static deformation is effective in increasing the relative densities of the single and multi-layer samples. A relatively higher density is also seen in Figure 5.1 for single layer Al samples before and after quasi-static deformation, while single layer 20% SiC samples show relative lower densities as compared with single layer samples of Al and 10% SiC. The relative densities of multi layer samples are also comparable with those of Al and 10%SiC single layer samples and the relative densities of single and multi layer samples, after quasi-static deformation, are higher than 98% except 20% SiC single layer sample as depicted in Figure 5.1.

The reduced relative densities of the single layer composite samples as compared with Al sample before and after quasi-static deformation is likely due to the lack of inelastic deformation capability of the SiC particles, leading to insufficient plastic deformation for the enclosing of the porosities which are presumably existed between matrix-particle interfaces. The plastic deformation may also induce damage accumulation in the form of matrix voiding and cracking and particle cracking which have reverse effect on the relative densities of the composite single samples. Before testing of samples the sample surfaces and sides were carefully checked for the visible macro-cracks and none was found. Few of the samples were also cut through cross-section and prepared metallographically for microscopic observations. Again no cracks were observed in polished surfaces.
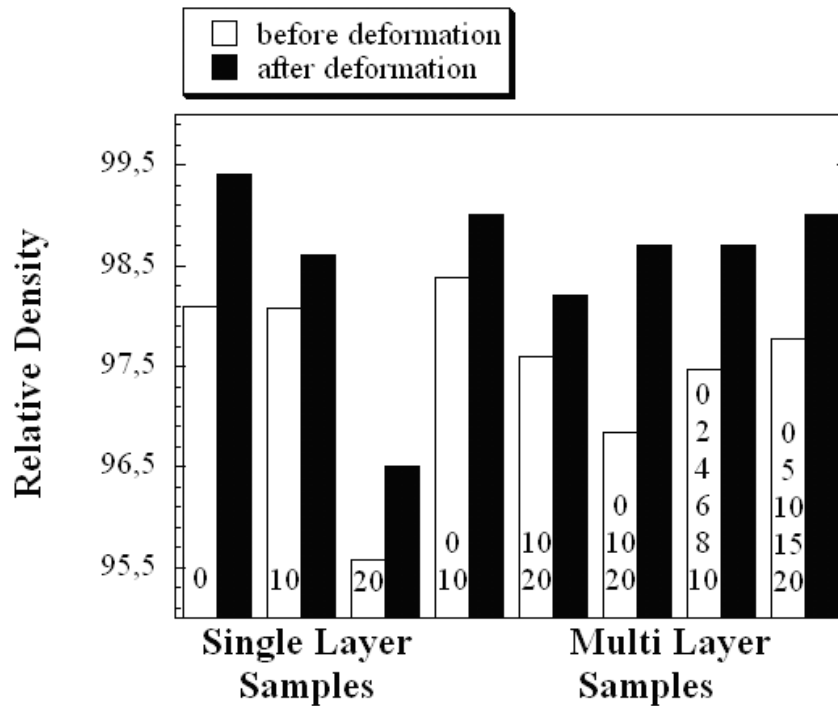
Figure 5.1 Relative densities of single and multiple layer samples before and after quasi-static deformation.

6.2 Quasi-static Tests

6.2.1 Single-layer Samples

At least 5 tests were conducted for each single layer sample and the resulting true stress- strain curves of the quasi-statically tested single layer samples are shown sequentially in Figures 5.2, 5.3 and 5.4 for 0%, 10% SiC and 20% SiC samples. For comparison purpose true-stress-strain curves of the selected 0%, 10% SiC and 20% SiC samples are shown together in Figure 5.5. As shown in these curves, single layer samples show typical elastic-plastic behavior; a linear elastic region is followed by an inelastic deformation region with a strain hardening rate slightly decreasing with strain. The effect of SiC-addition is to increase the yield strength, strain hardening rate after yielding and flow stresses (Figure5.5).
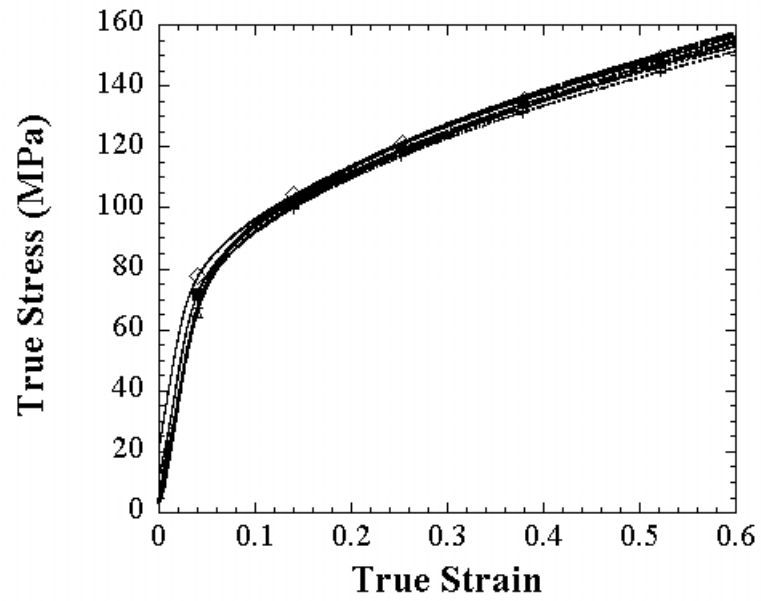
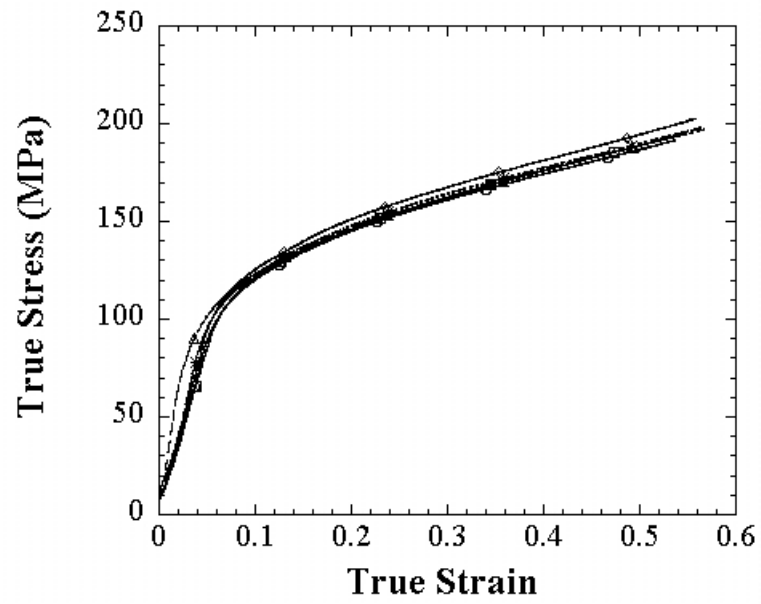**Figure 5.2** True stress-strain curves of Al samples.

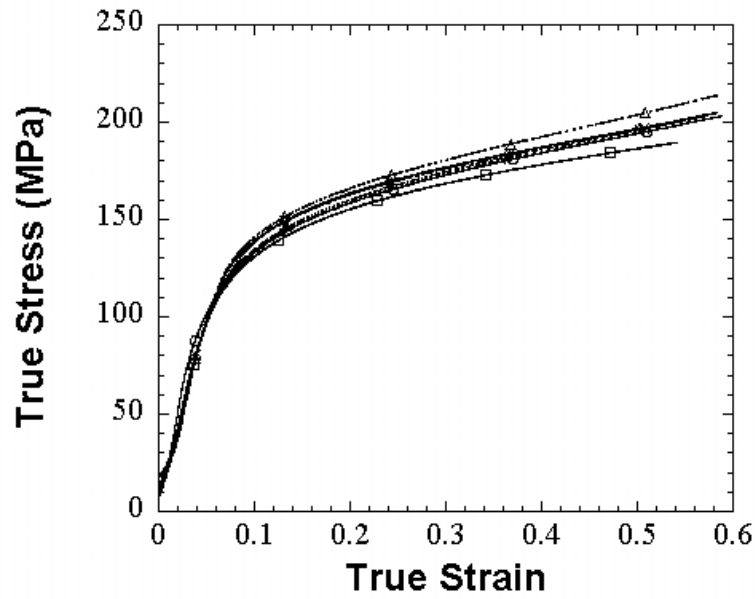**Figure 5.3** True stress-strain curves of 10% SiC composite samples.

Figure 5.4 True stress-strain curves of 20% SiC composite samples.
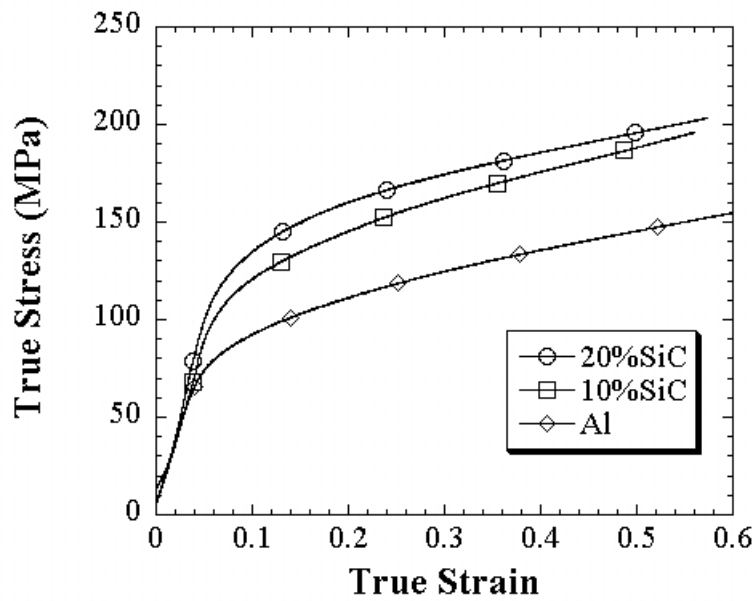

Figure 5.5 Representative true stress-strain curves of single layer samples.

6.2.2 Multi-layer Samples

True stress *vs.* true strain curves of the prepared multi-layer samples of 0/10, 10/20, 0/10/20, 0/5/10/15/20 and 0/2/4/6/8/10 are shown sequentially in Figure 5.6 through Figure 5.10. Two layer sample of 0/10 shows stress-strain curves between 0 and 10% SiC (Figure 5.11) while 10/20 samples show stress values higher than those of

10%SiC and 20%SiC single layer samples (Figure 5.12). In three layer sample, 0/10/20, in which the average SiC particle volume fraction is 10%, the stress-strain curve perfectly matched to the stress-strain curve of the 10% SiC single layer composite (Figure 5.13). Between two and three layer samples the highest stress values are found in 10/20 two-layer sample (Figure 5.14). This is partly due to the higher average volume fraction of SiC particles in the 10/20 sample, 15%. In 0/10 and 0/10/20 samples the average SiC volume fractions are 5 and 10% respectively. Compared to 6 layer samples, 5 layer samples show higher values of stress, which is again partly due to the higher average SiC particle content of the 5 layer sample (Figure 5.15). In 0/5/10/15/20 samples the average SiC volume fraction is 10%, while in 0/2/4/6/8/10 sample it is 5%. Figure 5.16 shows the typical stress-strain curves of the layered samples for the comparison purpose. It is noted in this figure, the average SiC particle volume fraction is the dominant factor in determining the stress-strain behaviors of the layered samples. The lowest stress values are found in 0/10 samples (5% SiC) and the highest stress values in 10/20 samples (15% SiC).
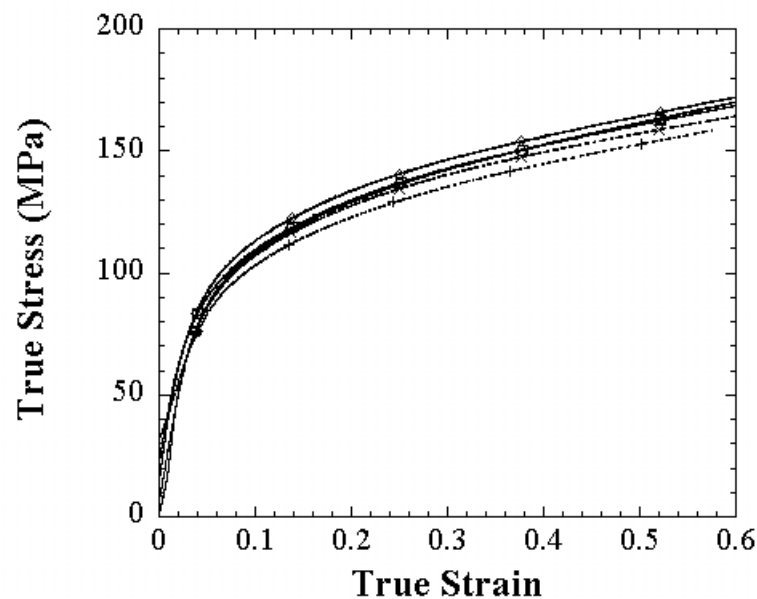

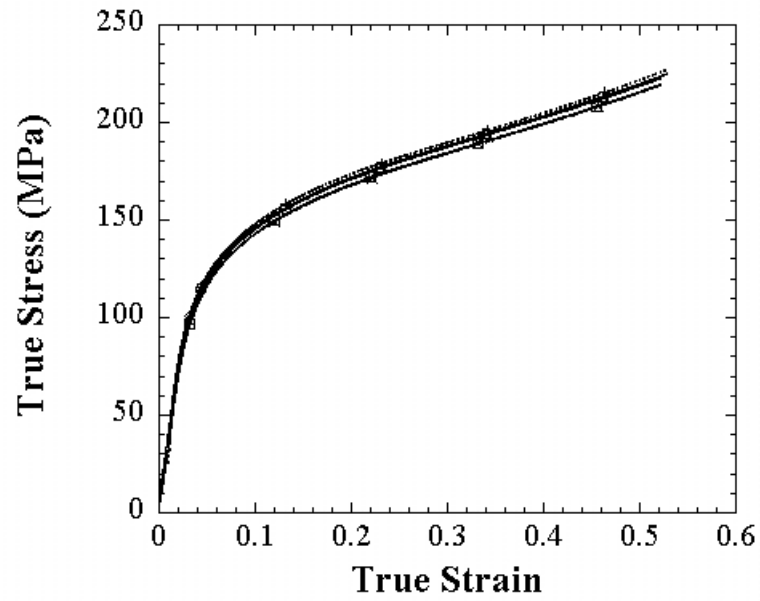**Figure 5.6** True stress-strain curves of (0/10) 2 layer samples.

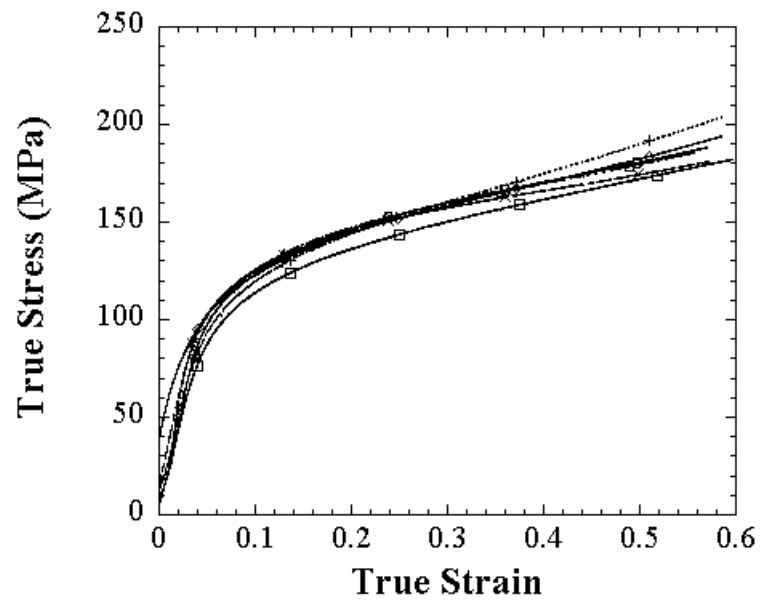**Figure 5.7** True stress-strain curves of (10/20) 2 layer samples.

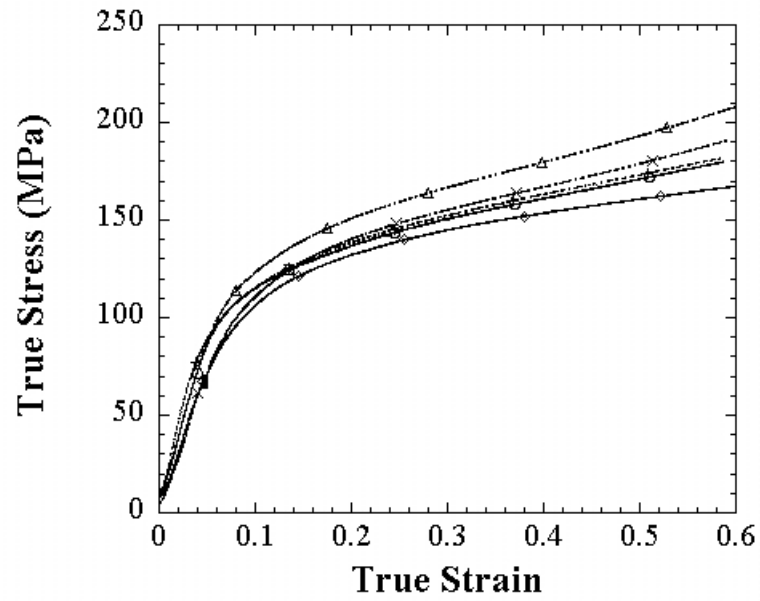**Figure 5.8** True stress-strain curves of (0/10/20) 3 layer samples.

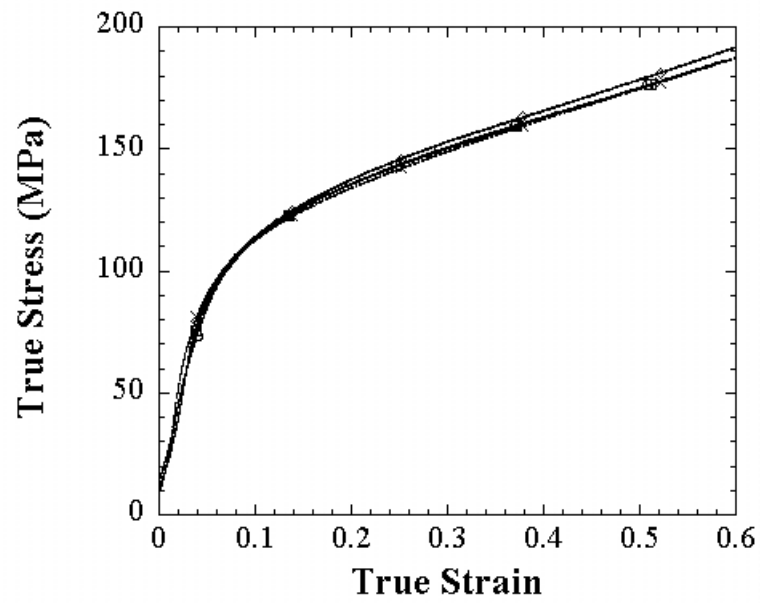**Figure 5.9** True stress-strain curves of (0/5/10/15/20) 5 layer samples.

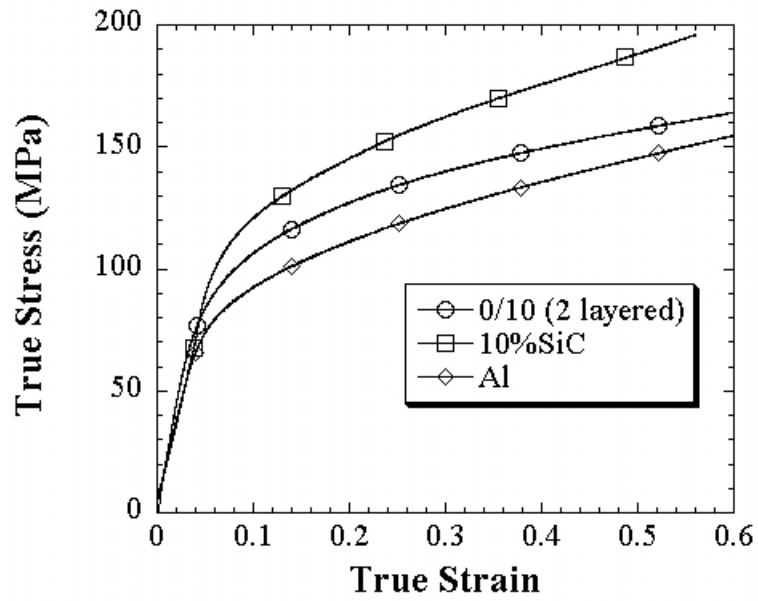**Figure 5.10** True stress-strain curves of (0/2/4/6/8/10) 6 layer samples.

Figure 5.11 Comparison of (0/10) with the related single-layer samples.
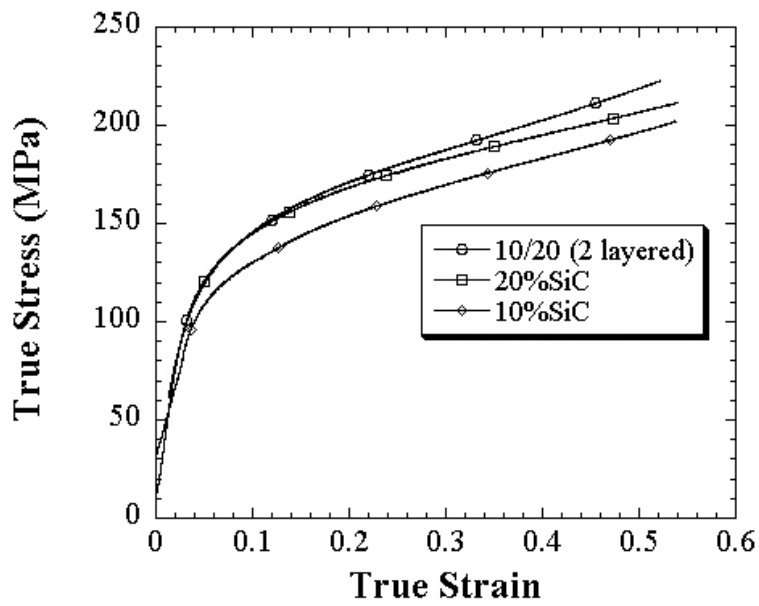

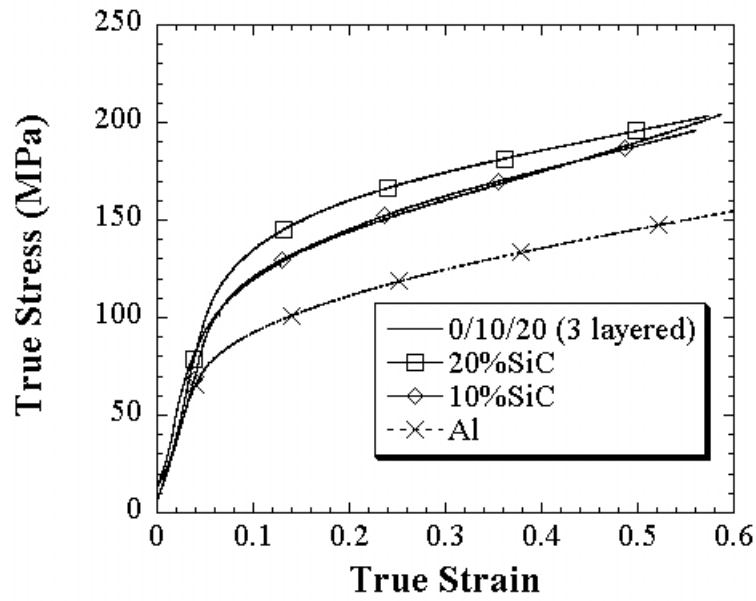**Figure 5.12** Comparison of (10/20) with the related single-layer samples.

Figure 5.13 Comparison of (0/10/20) with the related single-layer samples.
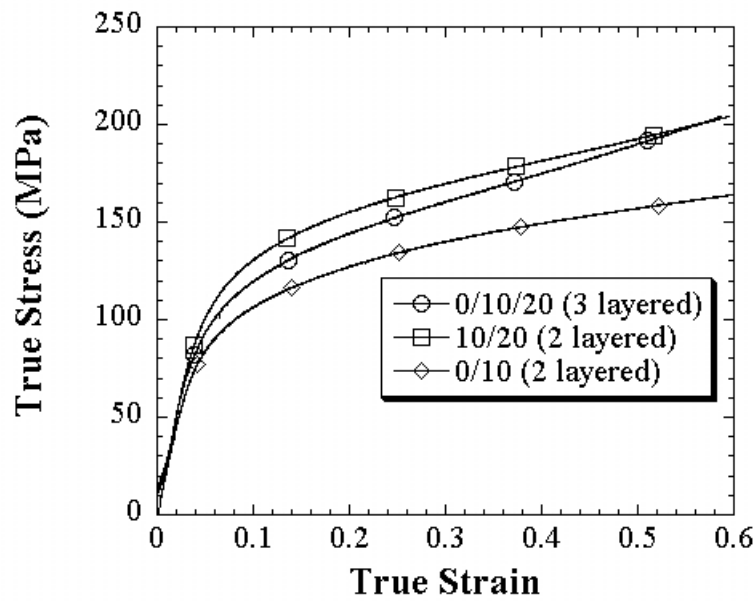
Figure 5.14 Comparison of 2 and 3 layer samples.
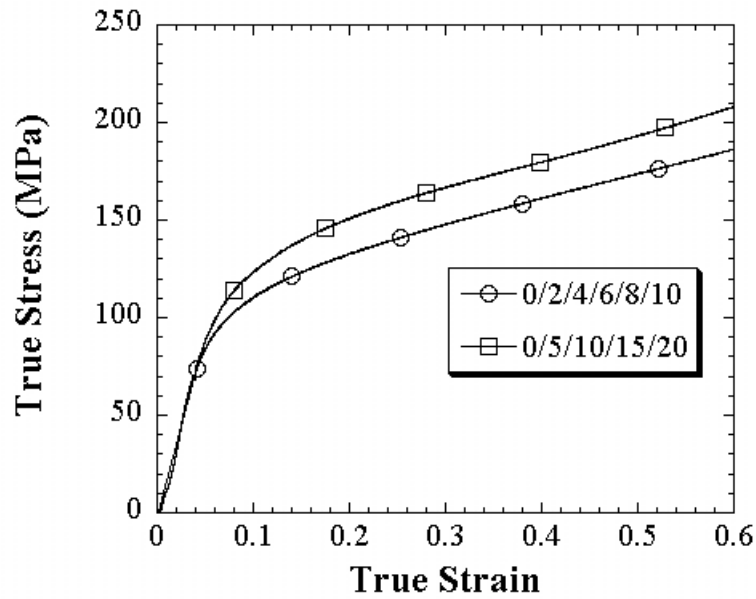
Figure 5.15 Comparison of 5 and 6 layer samples.
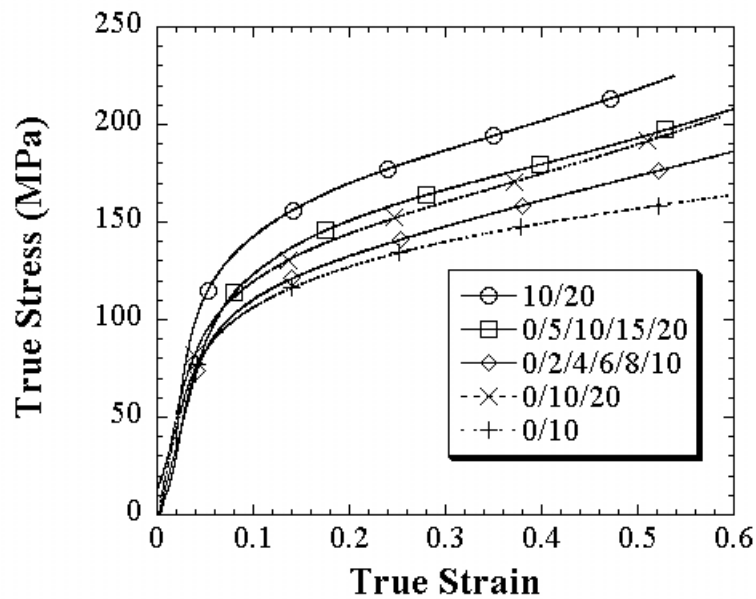
Figure 5.16 Comparison of all multi-layer samples.

Figure 5.17 shows the effect of SiC volume fraction on the flow stress corresponding to 10% strain in single layer samples. The flow stress increases from about 90 MPa to about 135 MPa as the SiC content increases from 0 to 20%. The increase in flow stress is about 40% with the increasing of SiC content from 0 to 20%. Figure 5.18 shows the flow stresses of multi layer samples as function of average SiC volume percentage. On the same figure, the fitted flow stress curve of the single layer

samples is also shown for comparison. Except 10/20 and 0/5/10/15/20 samples, the layered samples show good matching to the flow stresses of the single layer samples.

Figure 5.17 Flow stress at 10% strain vs. % SiC content of single layer samples.

Figure 5.18 Flow stress at 10% strain vs. % SiC of layered samples.

The strengthening mechanisms in discontinuously reinforced MMCs may be due to [48]; dislocation strengthening due to differences in CTEs, residual stresses,
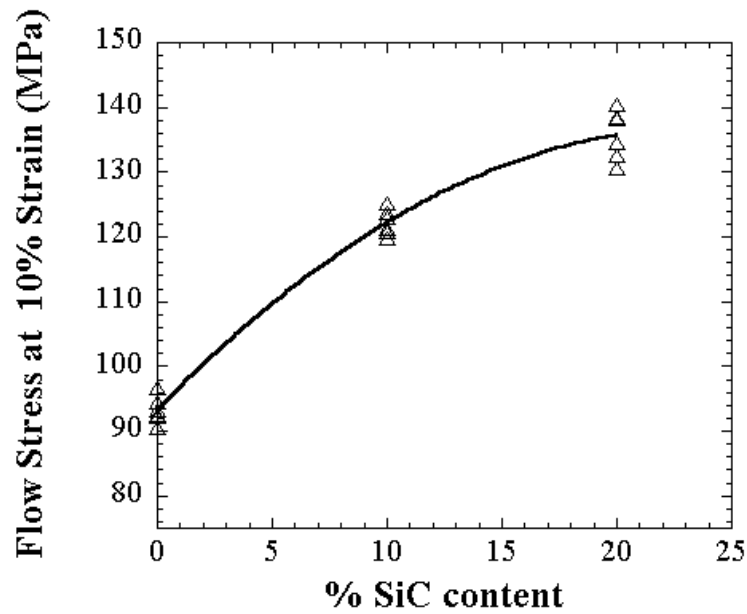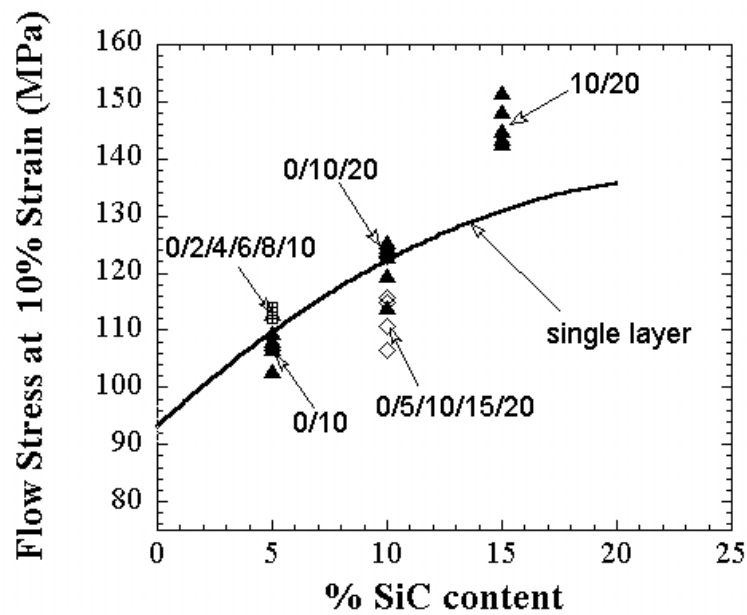
dispersion strengthening, grain size refinement, classical composite strengthening by load transfer.

The difference in coefficient of thermal expansion (CTE) between matrix and particle results in internal stresses as the composite cools down from the elevated temperature. Part of these stresses is relieved by generation of dislocations and the remaining misfit gives rise to a build-up of tensile residual stresses in the matrix.

The strengthening due to small particles can be estimated using the Orowan equation for bowing dislocations around particles giving dislocation loops around them

$$\sigma = \frac{2Gb}{\chi} \qquad (5.1)$$

where χ is the distance between particles. The Orowan strengthening in MMCs is argued to be small due to the relatively large particle size and the distance between particles [49,50] The Orowan strengthening is calculated to be ~6MPa in a composite containing 3μm particles with 17Vf% [50]. However, it may be significant in the age hardenable matrices where residual dislocations may affect the precipitate nucleation rate and size [49].

The MMCs usually have finer grain size as compared to monolithic alloys. The typical grain sizes in particulate and whisker reinforced MMCs are around 10μm [50]. The strengthening due to grain size refinement in composite can be determined using the Hall-Petch equation

$$\Delta\sigma_G = k_y d_g^{-\frac{1}{2}} \qquad (5.2)$$

where k_y is a constant and d_g is the grain size. The grain size refinement is calculated to be significant in MMCs containing grain sizes in the order of 1-10μm [50]. The contribution from subgrains near to the reinforcement can be also predicted using the Hall-Petch Equation.

For the prepared composites the residual stresses and classical load transfer through the particles are beleived to be the most effective in increasing the flow stress of the composite.

6.3   Prediction of Quasi-static Compression Behavior of Multi-layer Samples

The quasi-static compression behavior of three multi-layer samples, 0/10, 10/20 and 0/10/20 are predicted by using quasi-static test data of the related single-layer samples; Al and 10% and 20% SiC composites. When a multi-layer sample is subjected to an axial load as shown in Figure 5.19(a), based on the *equal-stress condition*, the stress (σ) of the multi-layer sample, would be equal to stress in individual layers and assuming a perfect bounding between layers, the strain (ε) of the sample would be equal to the sum of the strains of the individual layers, ε_1 and ε_2. That is;

$$\varepsilon = \varepsilon_1 + \varepsilon_2 \tag{5.3}$$

Single layer samples which have the same volume percent of reinforcement (SiC) with the individual layers of the multi-layer samples have stress and strain values σ_A, σ_B and ε_A, ε_B respectively (Figure 5.19(b) and (c)). Since the lengths of multi-layer sample and the single-layer samples are equal and lengths of the individual layers of the multi-layer sample are equal to each other,

$$\varepsilon_1 = \frac{\varepsilon_A}{2} \text{ and } \varepsilon_2 = \frac{\varepsilon_B}{2} \tag{5.4}$$

Putting Equation (5.4) into Equation (5.3),

$$\varepsilon = \frac{1}{2}\left(\varepsilon_A + \varepsilon_B\right) \tag{5.5}$$
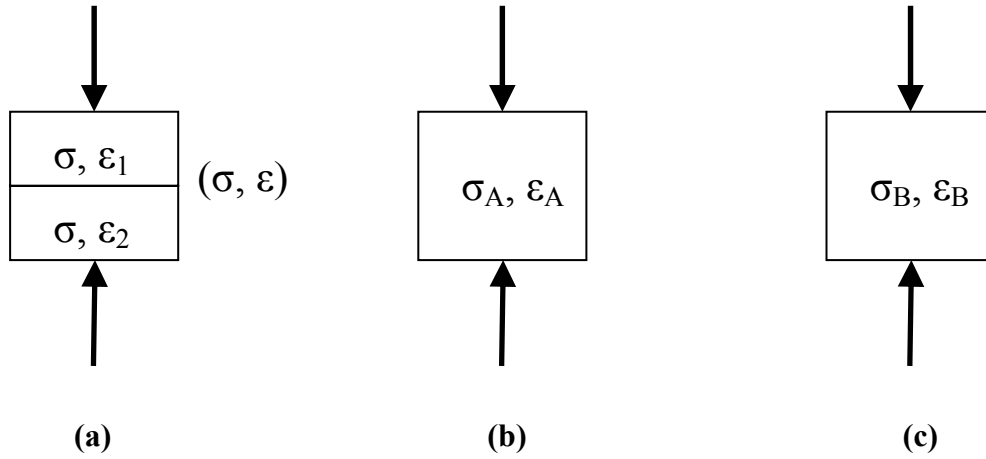
Figure 5.19 Schematics of, (a) multi-layer sample, (b) & (c) single layer samples, under compression.

The true stress-strain curves of the single layer samples can be fitted by a power law equation [32],

$$\sigma_A = K_A \varepsilon_A{}^{n_A} \tag{5.6}$$

$$\sigma_B = K_B \varepsilon_B{}^{n_B} \tag{5.7}$$

where n is the strain-hardening coefficient. Equations (5.6) and (5.7) are valid from the beginning of the plastic flow. True stress-strain diagrams from the beginning of the plastic flow and the fitted power expressions for the single-layer samples Al, 10% and 20% samples are given in Figures 5.20, 5.21 and 5.22 respectively. If the strains ε_A and ε_B in Equations (5.6) and (5.7) are put in Equation (5.3), one can obtain following equation for the strain of the multi-layer sample;

$$\varepsilon = \frac{1}{2}\left[\left(\frac{\sigma}{K_A}\right)^{\frac{1}{n_A}} + \left(\frac{\sigma}{K_B}\right)^{\frac{1}{n_B}}\right] \tag{5.8}$$

By inserting the experimental stress values (σ) of the quasi-static stress-strain curve of a multi-layer specimen in Equation (5.8), corresponding strain values (ε) can

be calculated. It should be noted that the prediction is based on the perfect matching interface between layers.
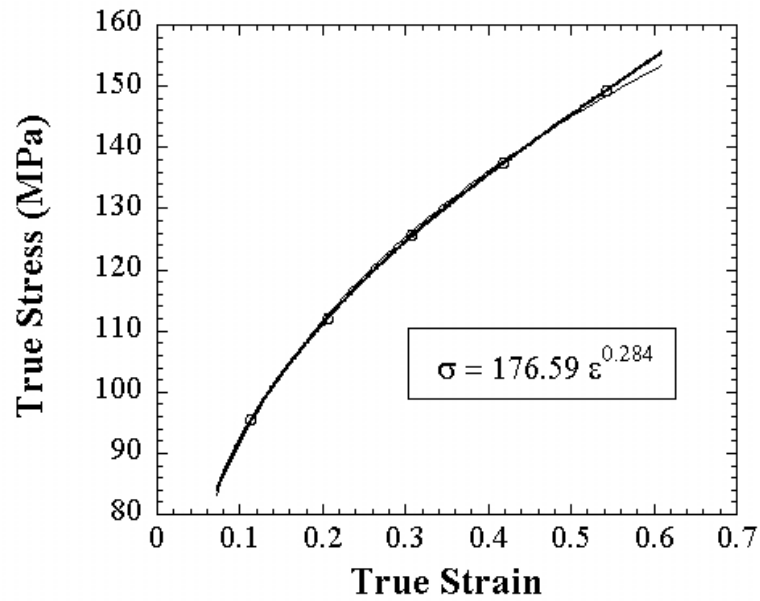

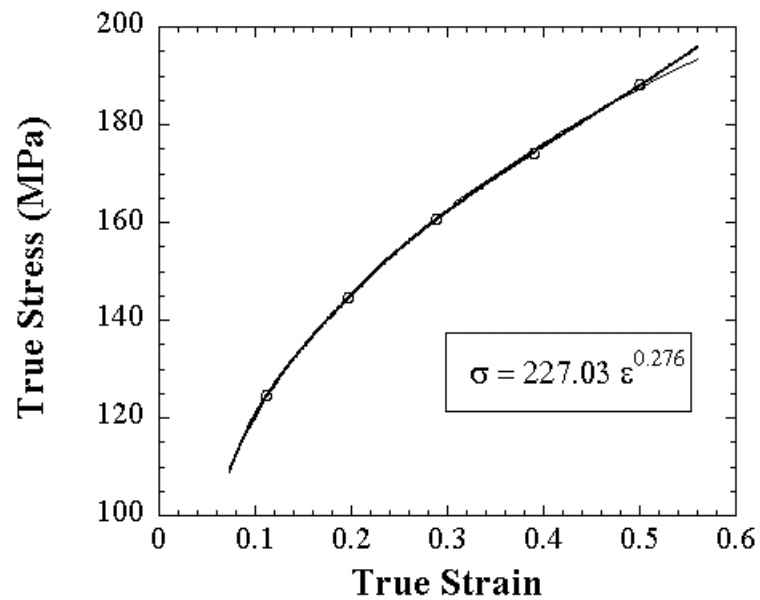**Figure 5.20** Fitting of stress-strain curve of Al sample to Equation (5.6).

Figure 5.21 Fitting of stress-strain curve of 10% SiC composite sample to Equation (5.6)
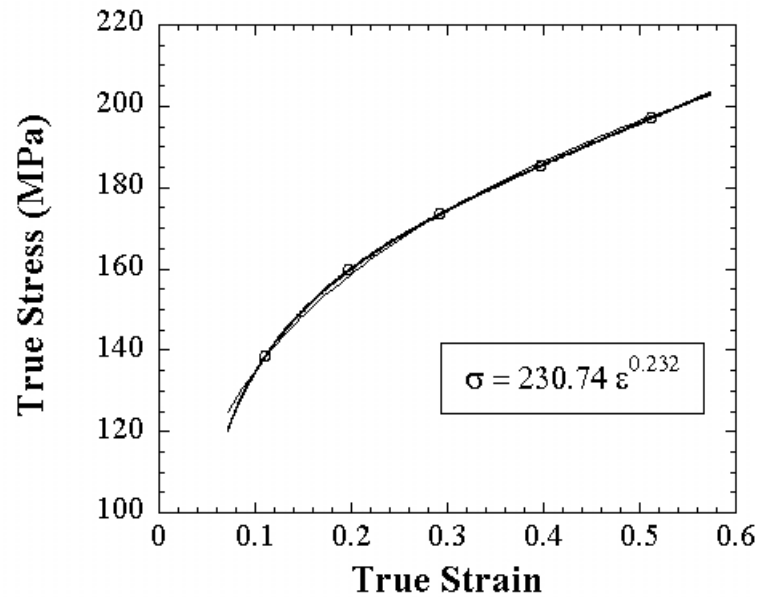
Figure 5.22 Fitting of stress-strain curve of 20% SiC composite sample to Equation (5.6).

By using Equation (5.8) and the power expressions for the single layer samples given in Figures 5.20, 5.21 and 5.22, predicted true stress-strain curves for the multi-layer samples 0/10, 10/20, 0/10/20 were drawn together with the experimental true stress-strain diagram of the multi-layer sample and true stress-strain diagrams of the corresponding single layer samples, in Figures 5.23, 5.24 and 5.25 respectively.

The quasi-static compression stress-strain behavior of multi-layer composite of 0/10 and 0/10/20 show quite well agreement with that of the predicted stress-strain behavior while 10/20 shows disagreements with prediction. In 10/20 composite multi-layer sample the experimental stress values are however higher than those of predicted values. The discrepancy between predicted and experimental stress values is partly due to the non-homogeneous deformation of layers because of the resistance provided by the adjacent layers. At the interface between the layers due to the Poisson's effect a complex state of stress occurs. At the same stress level, the lateral expansion of the Al and/or composite layer is prevented by the lower Poisson's ratio of the adjacent composite layer, resulting in a complex state of stress development leading to increases in stress levels of multi-layer materials. This effect can be easily seen in Figure 3.6 in which the higher-level deformation occurs in the midsections of the layers where the Poisson's effect becomes less effective.

Figure 5.23 Predicted and experimental stress-strain curve of 0/10 sample and experimental stress-strain curves of the corresponding single layer samples.

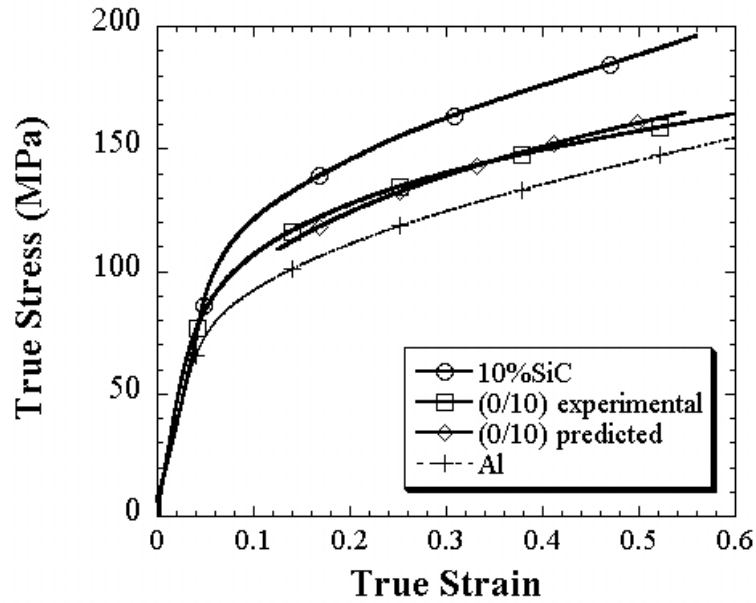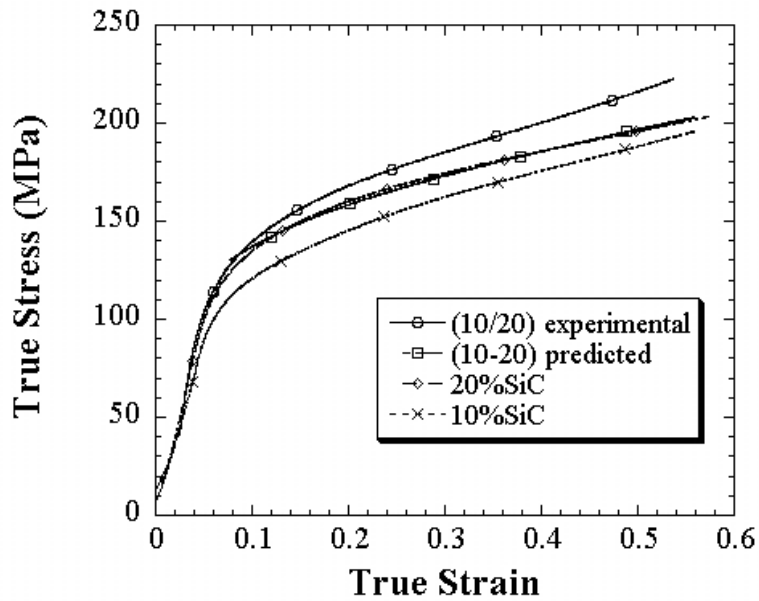**Figure 5.24** Predicted and experimental stress-strain curve of 10/20 sample and experimental stress-strain curves of the corresponding single layer samples.
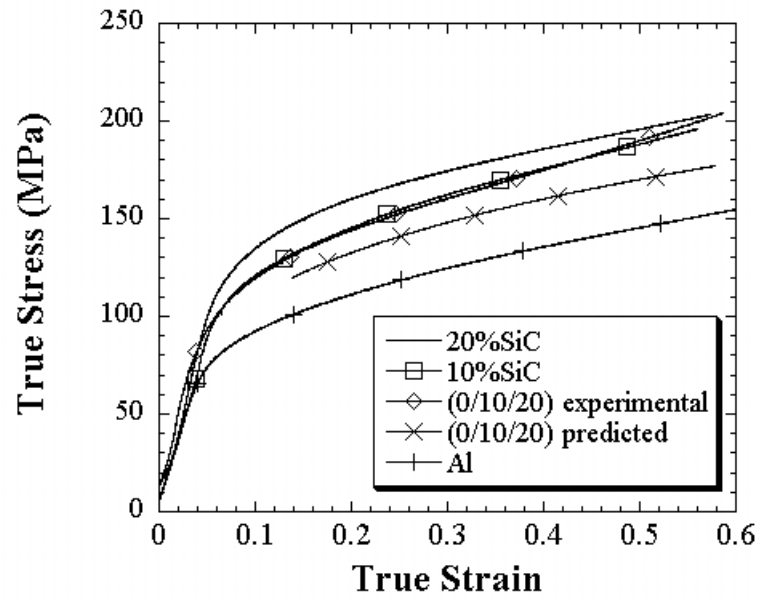
Figure 5.25 Predicted and experimental stress-strain curve of 0/10/20 sample and experimental stress-strain curves of the corresponding single layer samples.

6.4 High Strain Rate Tests

The data reduction of the high strain rate tests was carried out as explained in section 4.2.4. Single-layer samples were tested at three different outer chamber pressures of SHPB, namely 30, 60 and 90 psi corresponding to the strain rates of about 1000, 2000 and 3000 s^{-1} (Figures 5.26). Multi-layer samples were however tested at two different pressure values, 30 and 90 psi, corresponding to the strain rates of 1000 and 3000 s^{-1} (Figure 5.27). Since the strain rate varied in each single test, an average strain rate was calculated. For a specific test, the instantaneous strain rate varied during deformation, from zero to final or failure strain, and therefore an average strain rate was calculated as

$$\dot{\varepsilon}_{avg} = \frac{1}{\varepsilon_f} \int_0^{\varepsilon_f} \dot{\varepsilon} \, d\varepsilon \qquad (5)$$

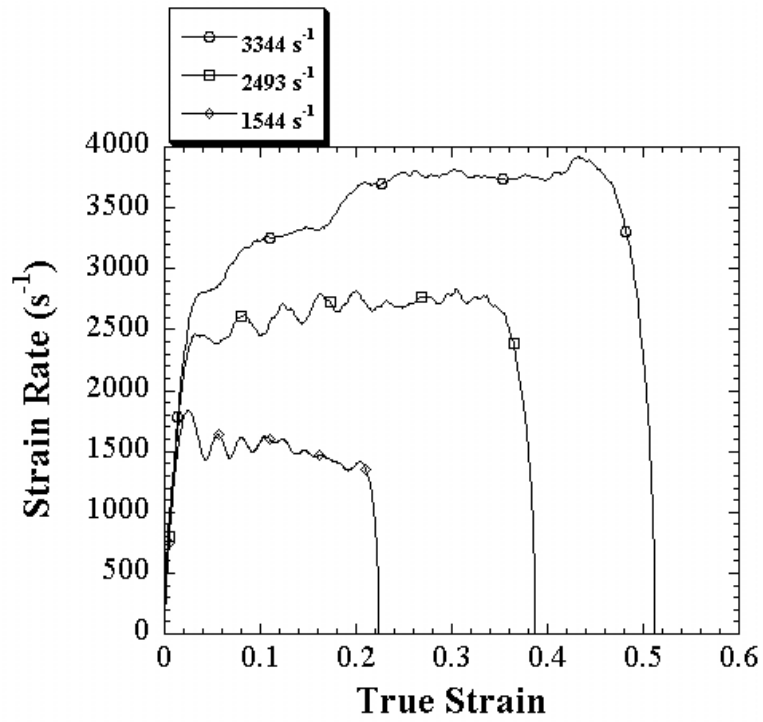where, ε_f is the maximum strain.

Figure 5.26 Strain rate vs. true strain in high strain test of Al sample at three different strain rates.
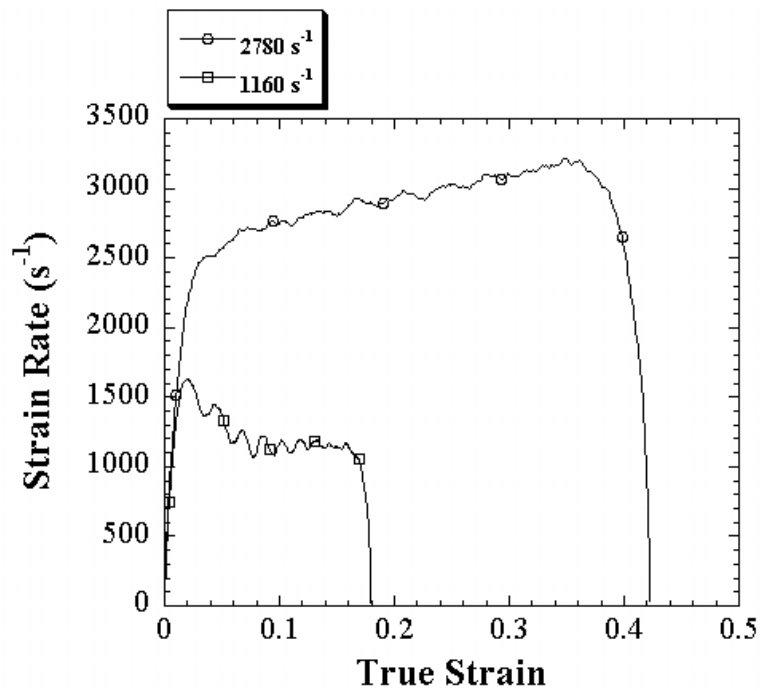

Figure 5.27 Strain rate vs. true strain in high strain test of 0/2/4/6/8/10 sample at three different strain rates.

Figure 5.28, 5.29 and 5.30 show the typical stress-strain curves of Al, 10% SiC and 20% SiC single layer samples at 3 different high strain rates, respectively. As noted in these figures, higher the strain rate higher the final strain attained by the samples. Similar to the quasi-static tests, composite single layer samples show higher flow stresses than Al single layer sample as depicted in Figure 5.31. The flow stress values of 0/10 samples, as in the case of quasi-static test, are found to be between the stress values of Al and 10%SiC single layer samples (Figure 5.32). Contrary to quasi-static tests, high strain rate tests result in a reduced flow stress behavior in 10/20 samples; the stress values are found between 10 and 20% SiC single layers (Figure 5.33). The strain rate is most effective in increasing stress values of 0/10/20 samples and stress values are found to be higher than 20% SiC single layer composite sample (Figure 5.34).

Figure 5.35 shows the stress-strain curves of 2 and 3 layer samples at the highest strain rates for comparison purpose. As shown in this figure the stress values of 0/10/20 samples are higher than 10/20 samples, which is contrary to the quasi-static tests.
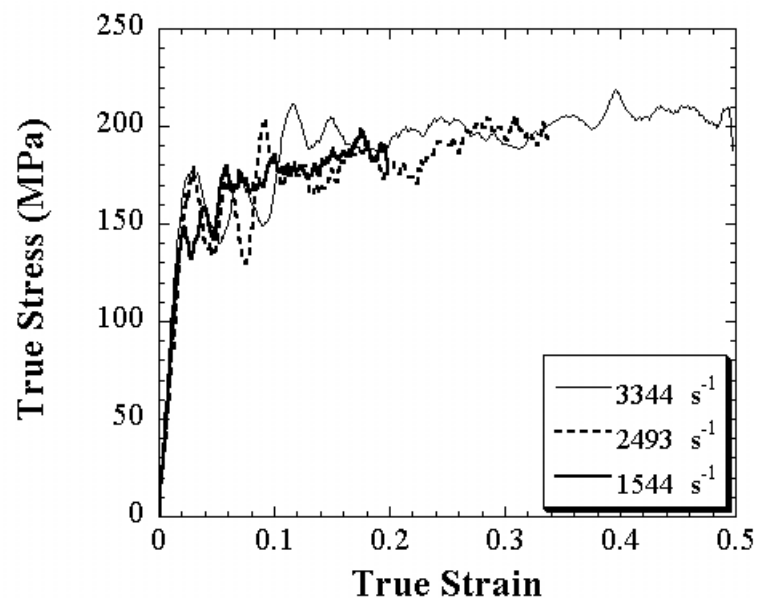
Figure 5.28 True stress-strain curves of Al at different strain rates.
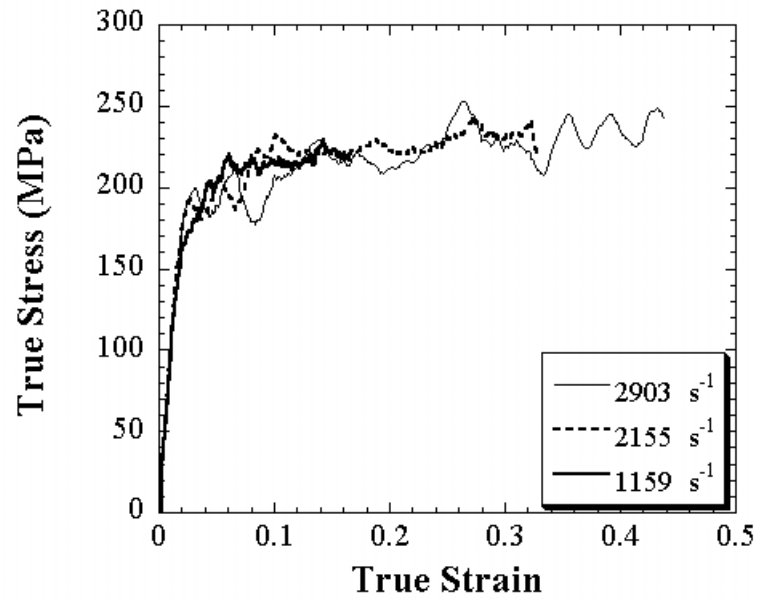
Figure 5.29 True stress-strain curves of 10% SiC at different strain rates.
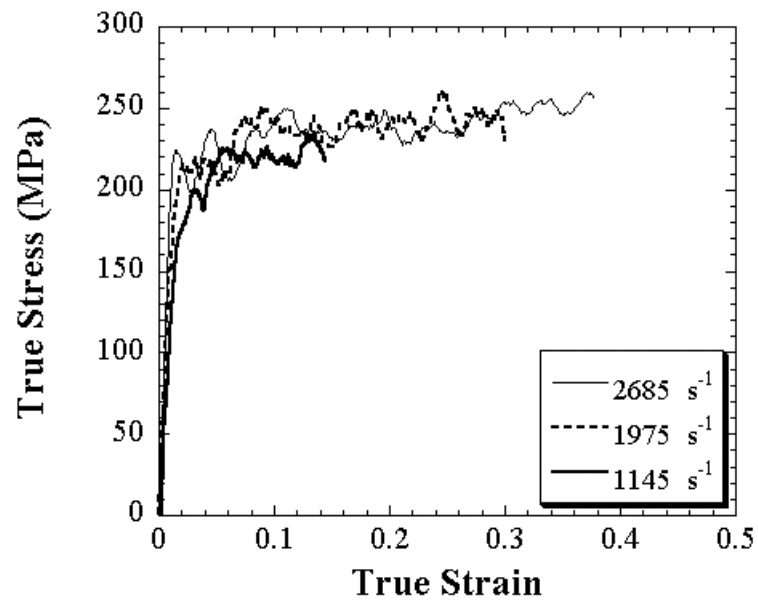
Figure 5.30 True stress-strain curves of 20% SiC at different strain rates.
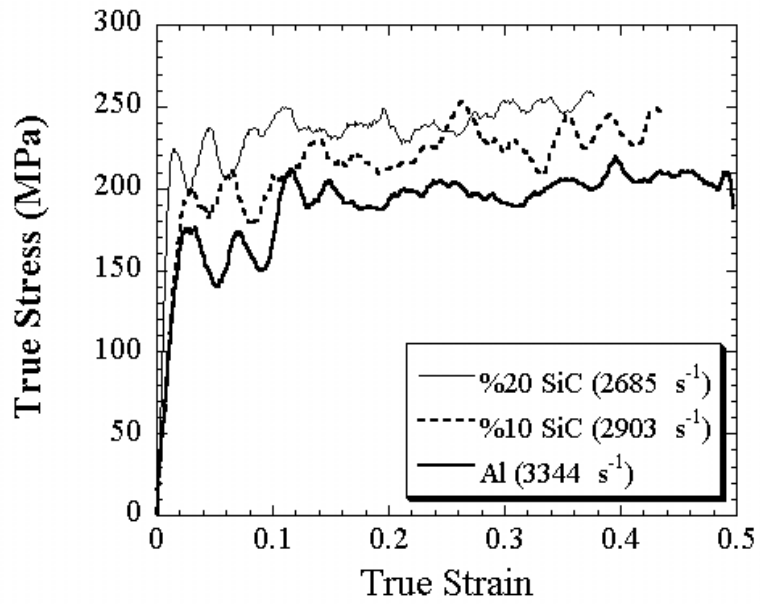
Figure 5.31 Comparison of single layer samples.
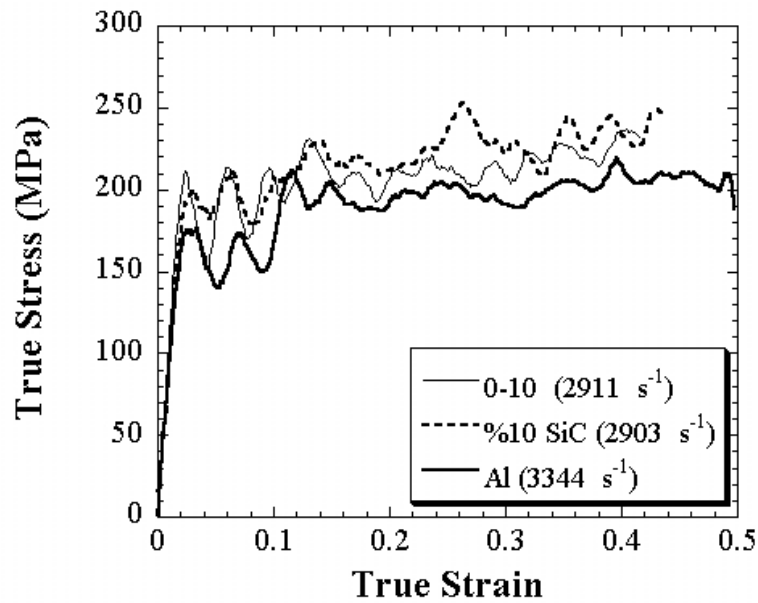
Figure 5.32 Comparison of stress-strain curves of 0/10 sample with the related single layer samples.
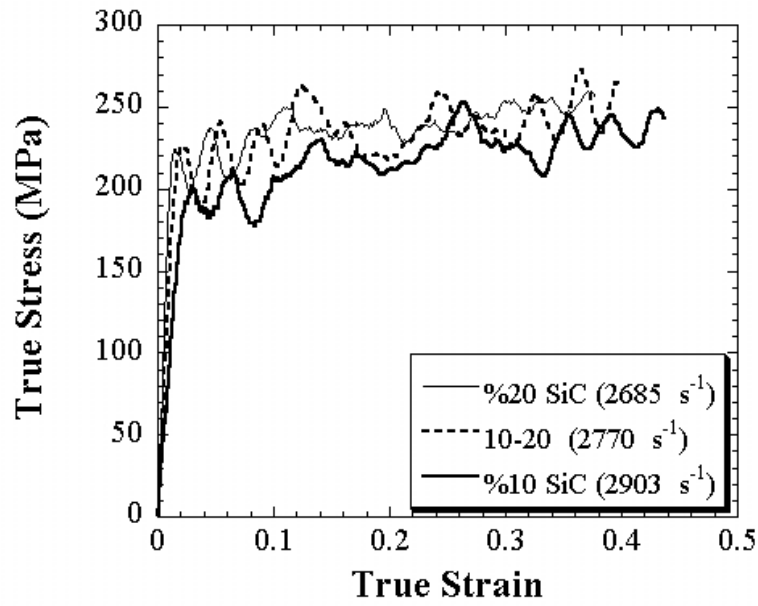
Figure 5.33 Comparison of stress-strain curves of 10/20 sample with the related single layer samples.
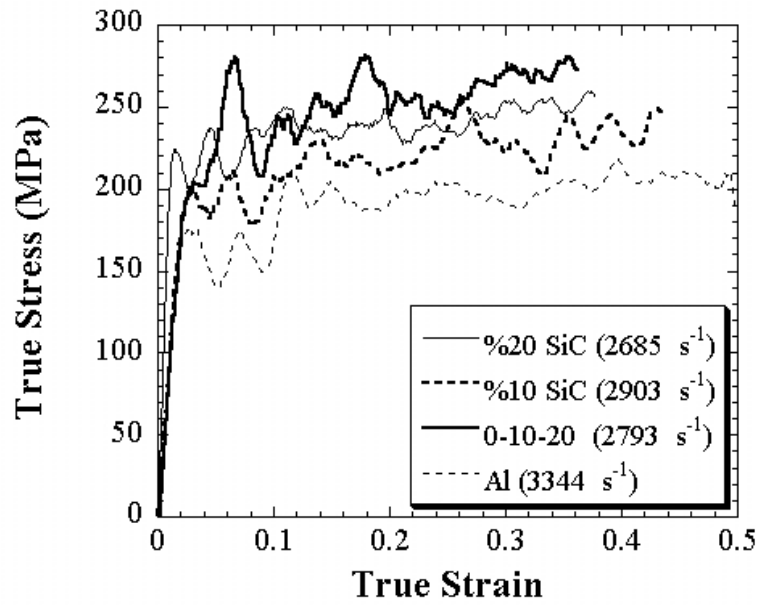
Figure 5.34 Comparison of stress-strain curves of 0/10/20 sample with the related single-layer samples.
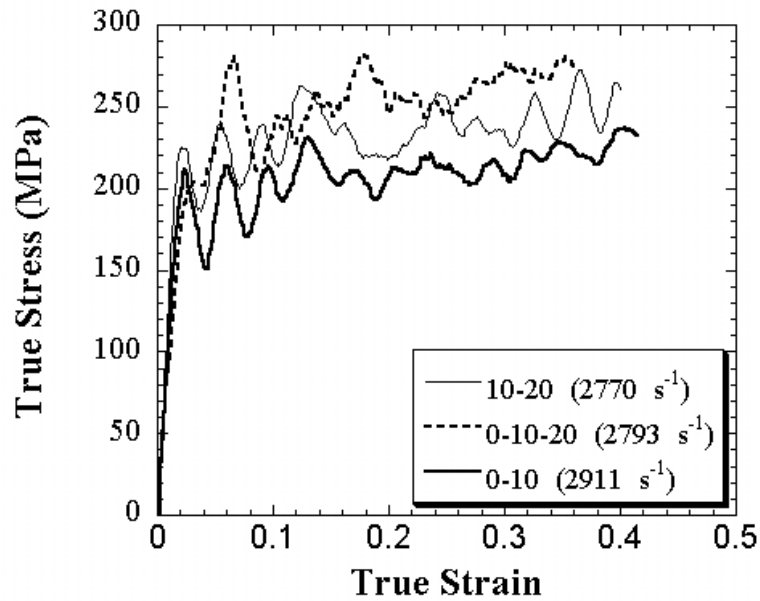
Figure 5.35 Comparison of stress-strain curves of 2 and 3 layer samples.

In the testing of 5 and 6 layer samples, large oscillations in stress values especially at about 3000 s^{-1} are found in the stress-strain curves (Figures 5.36 and 5.37). Oscillations are also seen to be intensified in 0/2/4/6/8/10 samples. The large oscillations seen in the stress values are partly due to the wave reflections from the interfaces. It is also found that the stress values of 5 and 6 layer samples are very similar at high strain rates, although 5 layer samples show slightly higher stresses at low strains, Figure 5.38.
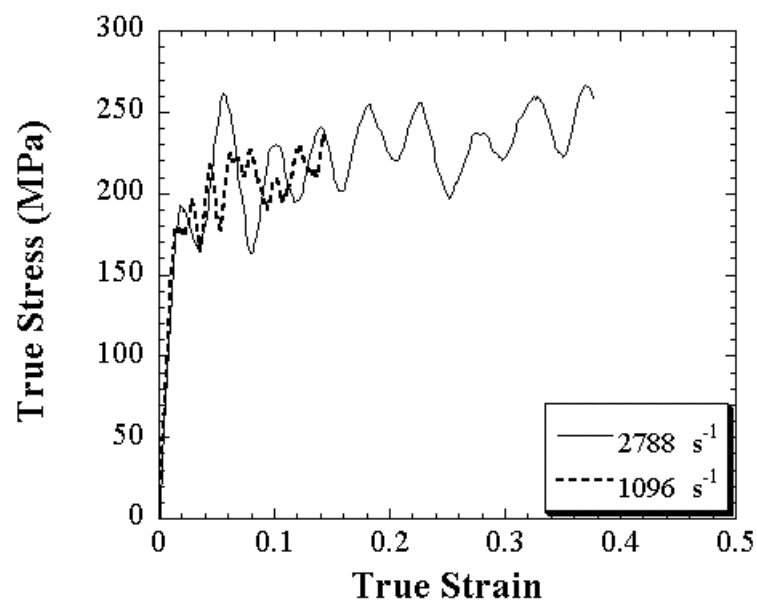
Figure 5.36 True stress-strain curves of 0/5/10/15/20 sample at different strain rates.
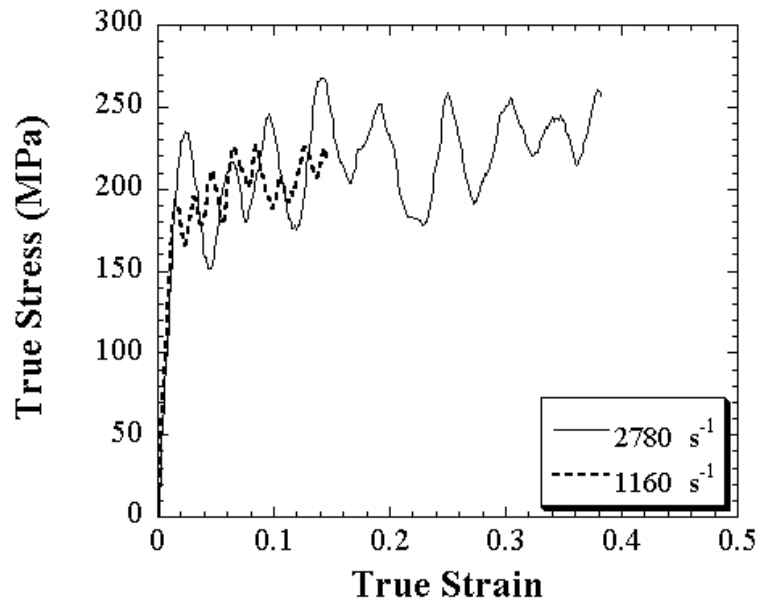
Figure 5.37 True stress-strain curves of 0/2/4/6/8/10 sample at different strain rates.
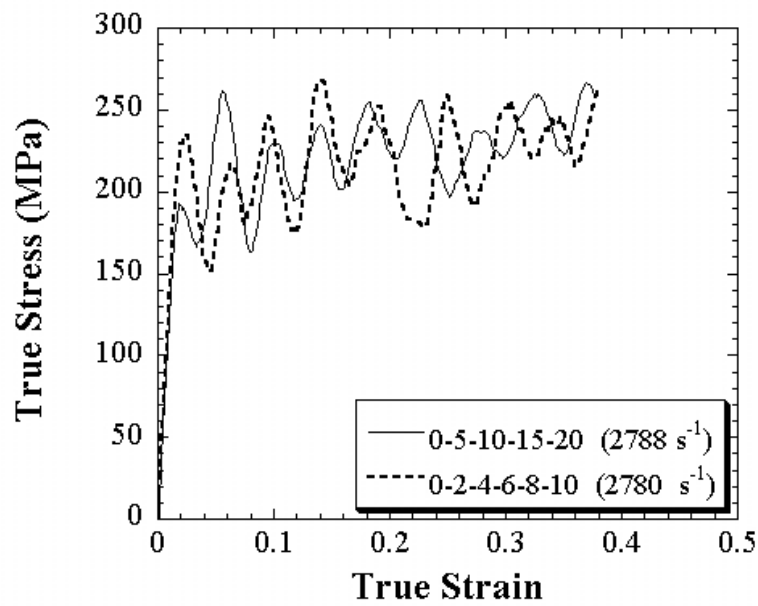
Figure 5.38 Comparison of stress-strain curves of 5 and 6 layer samples.

6.5 Effect of strain rate

The effect of strain rate on the flow stress values of the prepared samples was assessed applying following procedure. The quasi-static flow stress was determined from the quasi-static test as the final stress attained in the sample as depicted in Figure

5.39. The flow stress in high strain rate was taken as the yield strength as shown in Figure 5.39.

Figure 5.40 shows the variation of flow stress with the strain rate in single layer Al and 20% SiC samples. A linear interpolation to the data in this graph gives a slope, which corresponds to the strain rate sensitivity. Considering the scattering in flow stress data and the limited number of experiments, one can conclude that single layer samples of Al and composites show a similar strain rate dependency of the flow stress.

In the 0/10 and 0/10/20 samples, the strain rate sensitivities are also found to be in accord with that of the single layer Al sample as shown in Figure 5.41. In 10/20 samples however the flow stress decreased as the strain rate increased. A similar reduced flow stress in 5 layer samples are also found as depicted in Figure 5.42. In 6 layer samples however the strain rate sensitivity is similar to that of the single layer Al sample (Figure 5.42).

Figure 5.39 True stress strain curves of quasi-static and high strain rate tests and flow stresses.

Figure 5.40 The variation of flow with strain rate in Al and 20%SiC samples.
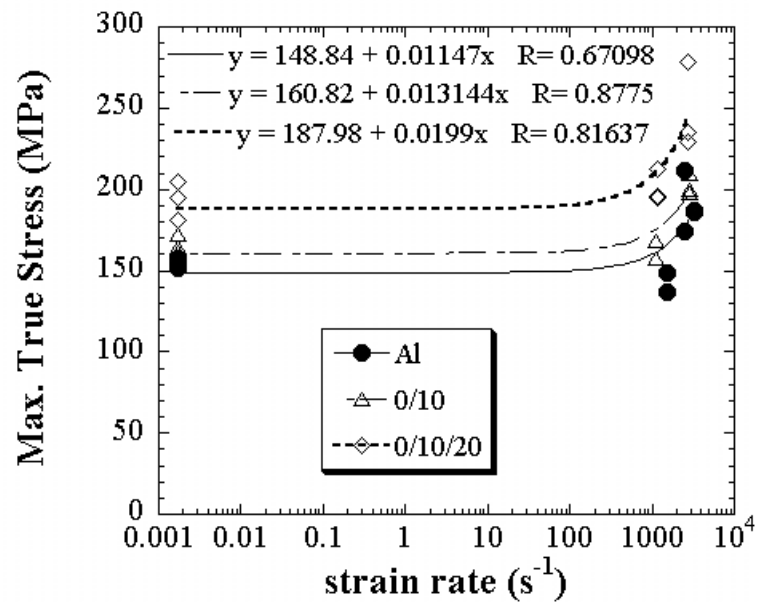
Figure 5.41 The variation of flow with strain rate in Al and 0/10 and 0/10/20 composite layered samples.
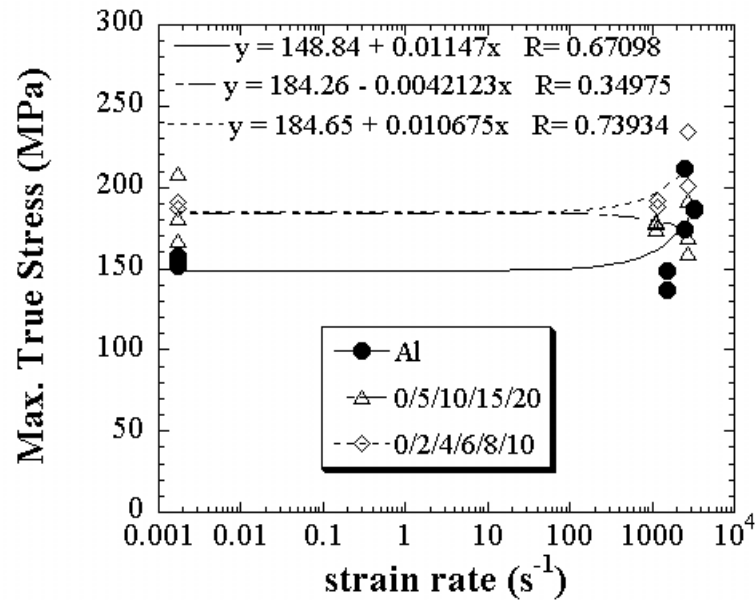
Figure 5.42 The variation of flow with strain rate in Al and 5 and 6 layered samples.

Common metallic materials such as Al [51] and Cu [52] have shown increased rate sensitive behavior at strain rates greater than $\sim 10^3$-10^4 s$^{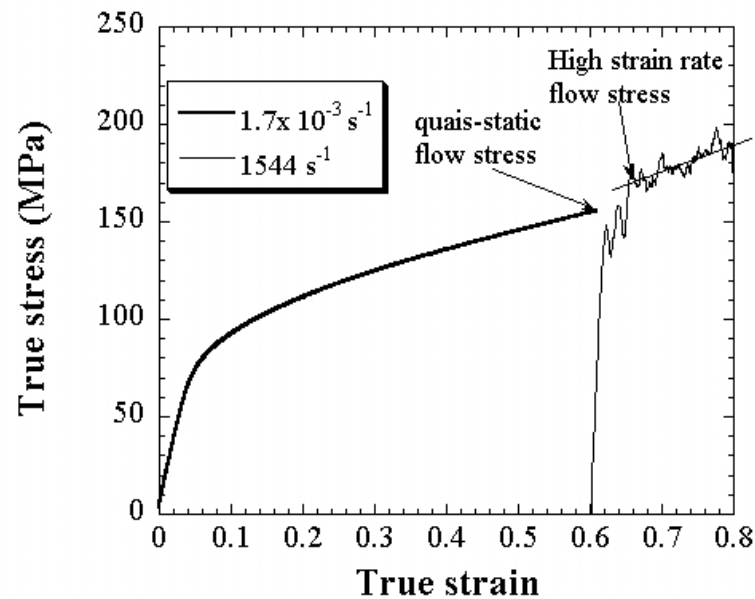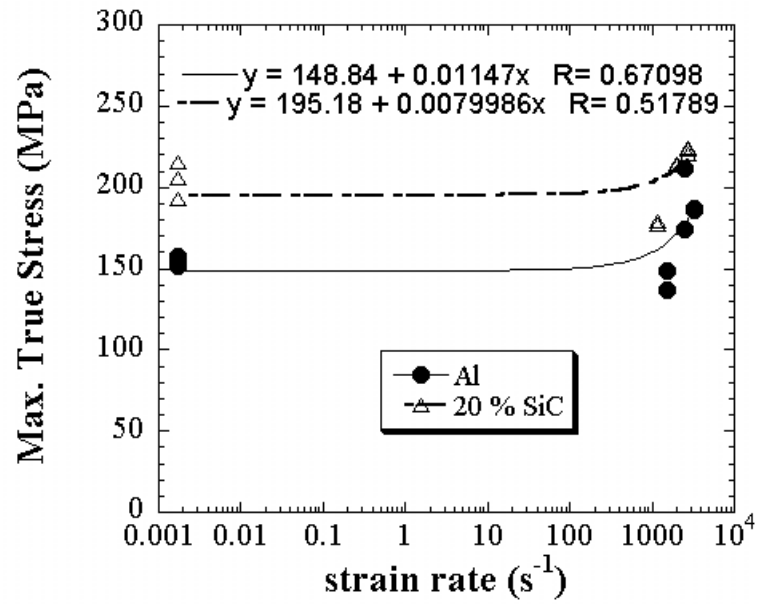-1}$, a behavior which is generally interpreted as a change of deformation mechanism from thermally activated to drag controlled. Below this critical strain rate range, little or no rate sensitivity is observed which is in accord with the present experimental results in which the increase in flow stress with strain rate is more pronounced at strain rates higher than 1000 s^{-1}.

Much of the high strain rate studies on metal matrix composites have been reviewed in references [53, 54]. The first experimental investigation of high strain rate behavior of MMCs is due to Harding *et al.* [55] and Marchand *et al.* [56]. Studies of the high strain rate behavior of specific MMCs include those of Perng *et al.* [57], Hong and Gray [58], Yadav et al. [59], Chichili and Ramesh [60], and Guden and Hall [61]. A higher strain rate sensitivity of the composite compared with matrix material has been generally found in these studies. Yadav *et al.* [59] numerically indicated that the effect of strain rate in particle reinforced MMCs would be strongly dependent on the particle volume fraction. Bao and Lin [62] and Yadav [59], based on axisymmetric unit cell model, showed that the effect of strain rate is coupled with the particle volume fraction and the strain rate hardening of the composite may be significantly higher than that of the matrix due to the constraining effect of particles. The strain rate in MMC's can reach very high local values at strain discontinuities present near the reinforcement. If the matrix alloy is itself rate sensitive at these locally attained strain-rates, the matrix

strength will increase significantly and lead to an observed increase in rate sensitivity of the composite relative to the unreinforced alloy at increasing strain rates. This effect was found to be pronounced at very high strain rates >3000 s^{-1} and therefore for the studied composites and layered samples any increases in the strain rate sensitivity as compared with Al could not be detected.

6.6 Microscopy

Table 5.1 summarizes failed specimens at high strain rates. Among the tested single layer samples, Al and 20% single layer samples did not show any failure while 2 samples of 10% SiC failed. In 3, 5 and 6 layer samples failure occurred through the separation of the first layer, Al, at the highest gas gun pressure corresponding to the strain rates of ~3000 s^{-1} (Figure 5.43, 5.44 and 5.45). SEM studies have shown that the SiC particles fractured during the separation of the interface (Figure 5.46). It was also found that during processing of MMC layers a thin oxide layer formed between the layers as shown in Figure 5.47. The formation of thin oxide layer is expected to be effective to reduce the bonding strength between the layers and therefore the failure occurred at the interfaces.

Table 5.1 Failed Specimens at High Strain Rates.

	Type	Number of Specimen	Test Pressures	Number of broken samples
Single-layer samples	Al	6	30,60,90	none
	10%SiC	6	30,60,90	2
	20%SiC	7	30,60,90	none
Multi-layer samples	0/10	5	30, 90	None
	10/20	5	30, 90	None
	0/10/20	6	30, 90	4 , 90psi (Al layer)
	0/2/4/6/8/10	4	30, 90	2 (90)
	0/5/10/15/20	6	30, 90	2 , 90psi (Al layer)
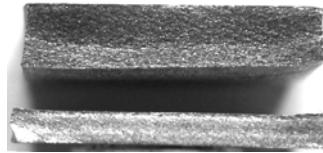
Figure 5.43 Separation at interface of 0/10/20 samples (0/10 interface).
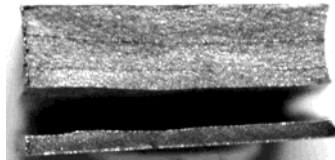
Figure 5.44 Separation at interface of 0/2/4/6/8/10 samples (0/2 interface).
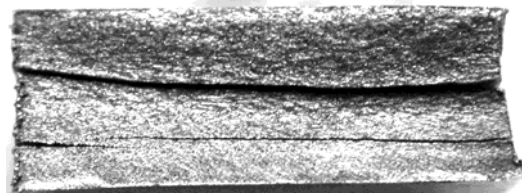
Figure 5.45 Separation at interfaces of 0/5/10/15/20 samples.
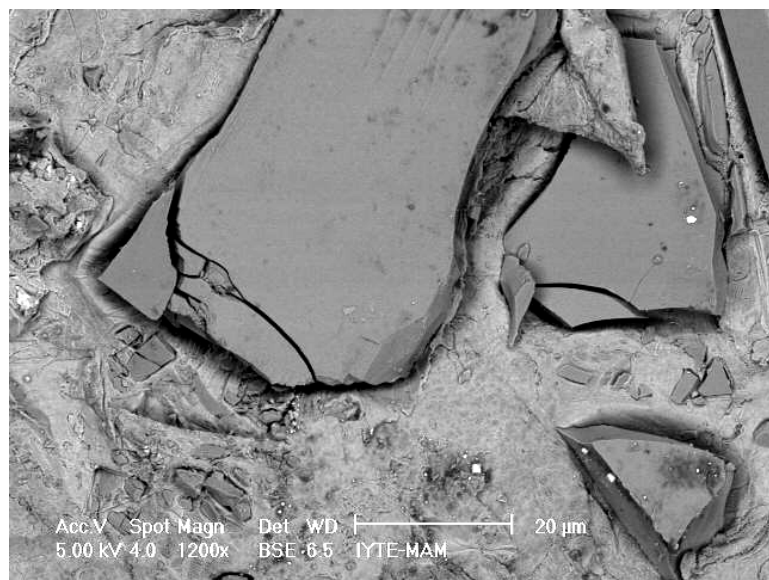
Figure 5.46 SEM images of the failed 0/10/20 sample 0/10 interface tested at 90 psi showing fractured SiC particles.
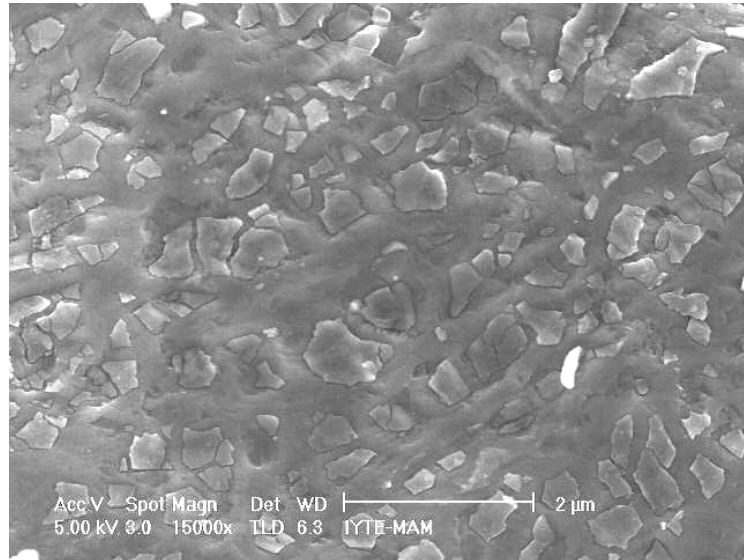
Figure 5.47 SEM images of the failed 0/10/20 sample 0/10 interface tested at 90 psi showing oxide plates.

The wave propagation in SHPB is quite complex. The compressive wave passing through the Al layer is reflected as a compressive wave at the interface with a higher impedance layer of the composite while it is reflected as a tensional wave from the specimen-bar interface. The compressive wave returned from the interfaces increases the magnitude of the compressive wave in the layer while the returned tensional wave tends to reduce the compressive wave. As the wave is reflected back and forth between the layers and between the specimen-bar interfaces, the analysis of the wave propagation becomes very difficult. But the failure in the first layer signaled that large compressive stresses occurred in the first layer or at the interface between Al and composite layer, which will be shown in the next section.

6.7   Modeling

Deformation profile and stress-strain behavior of a two layered sample (10/20) in high strain rate test is modeled using LSDYNA 3, with quarter symmetric SHPB model.

Figure 5.48 shows the 10/20 sample at initial state (t = 0 microseconds) before testing. Figure 5.49(a) shows the deformation profile of the sample at the final state

and Figure 5.71(b) is the photograph of a sample after high strain rate deformation. The final strain and deformation profiles of the modeled and tested samples show good coincidences.
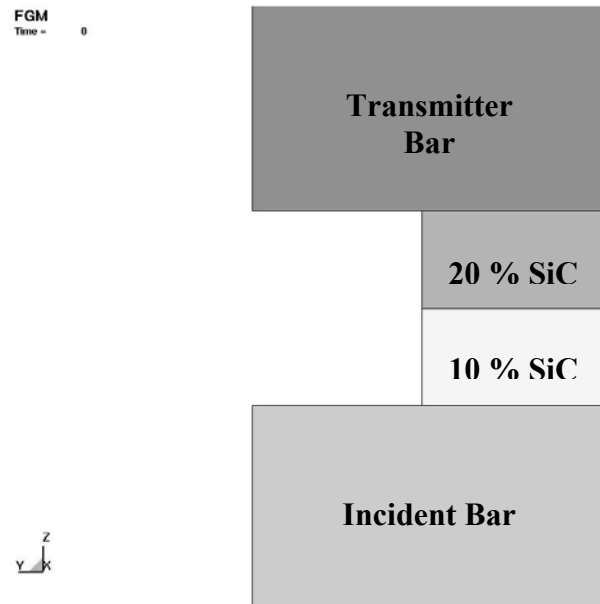
Figure 5.48 (10/20) 2-layer sample at t = 0 microseconds.
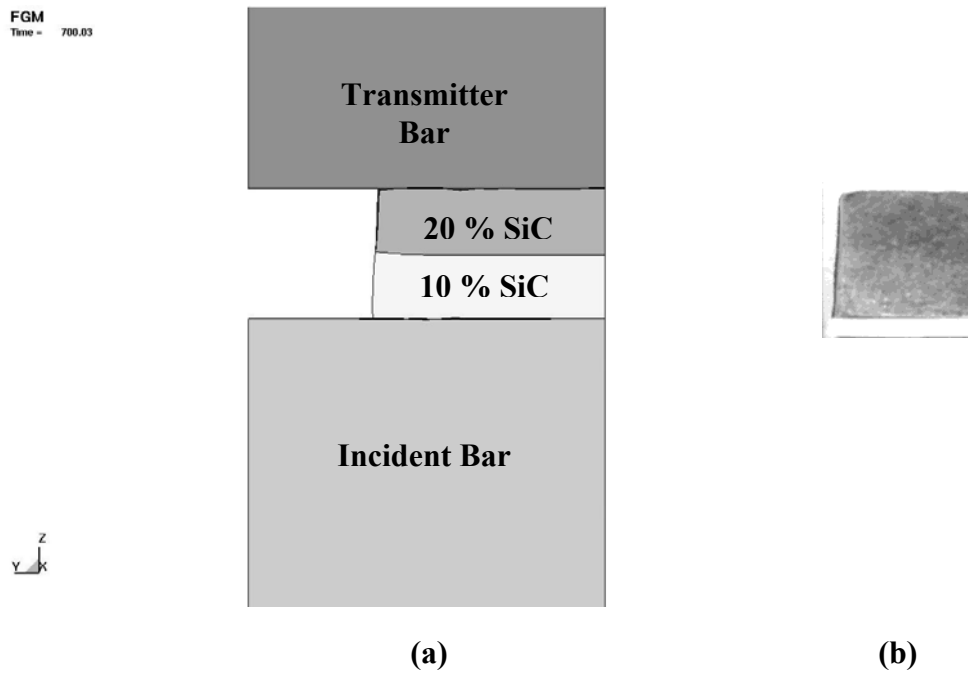
Figure 5.49 a) Simulated deformation profile, and b) photograph of the (10/20) sample after high strain rate test (t = 700 microseconds)

The stress-strain behavior of the (10/20) sample predicted by the model is compared with the experimental results in Figure 5.50. The model and experimental results show also good matching at low strains, while modeling results in higher stress values at increasing strain values. This may be due to the micro damage formation in layered sample and further investigation will be performed on this discrepancy.
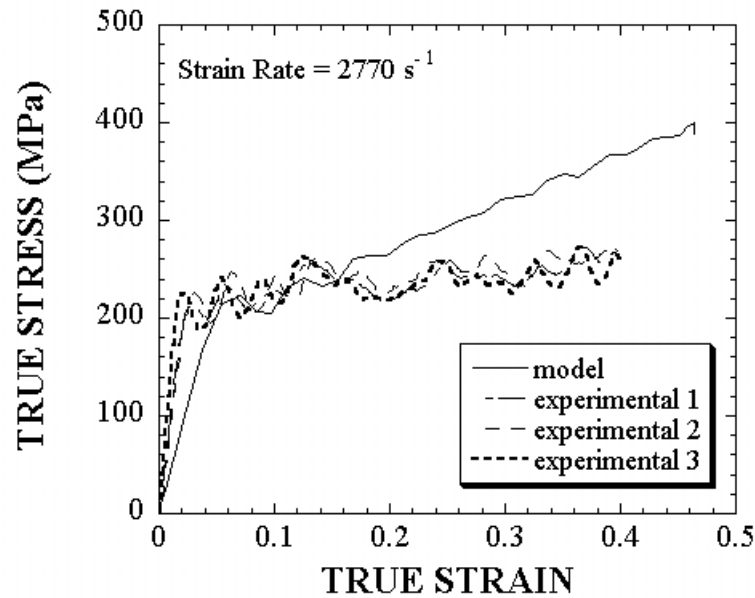
Figure 5.50 Stress-strain behavior of the (10/20) sample.

Stress on each layer was also predicted using the same model. The stress on the elements which are in the middle of each layer (10%SiC and 20%SiC reinforced layers) was calculated and the results, stress vs. time, are shown in Figure 5.51. As shown in Figure 5.51 higher stress level is found in lower impendence layer, 10% SiC.

As shown schematically in Figure 5.53 the compressive stress wave (incident wave) first passes through the 10% SiC reinforced layer. Since the impedance of the 20% SiC reinforced layer is higher than the that of 10% SiC reinforced layer the compressive wave partially reflects back as a compressive wave and the remainder transmits through the 20% SiC reinforced layer. Reflected compressive wave adds up with the incident compressive wave and increases the stress in the 10% SiC layer.
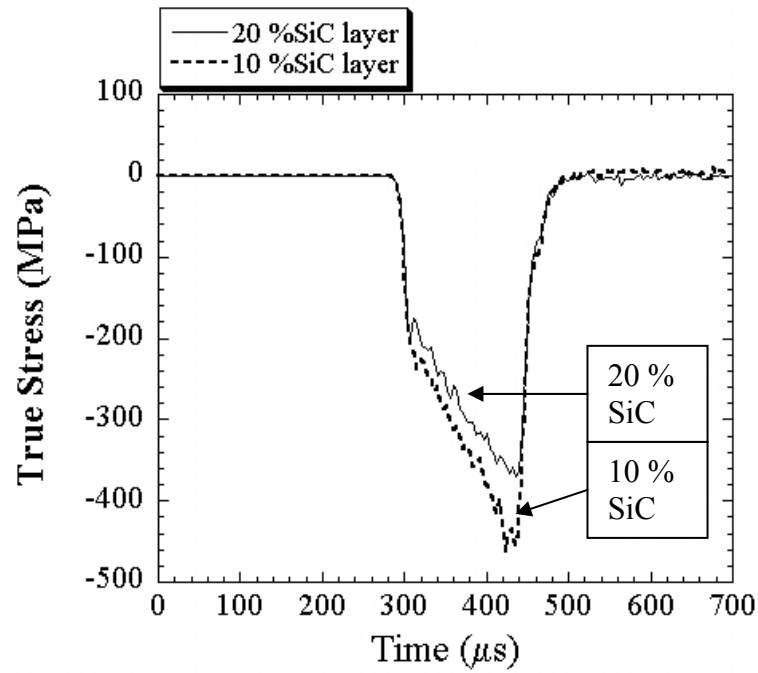
Figure 5.51 Stresses on the 10% and 20% SiC layers.
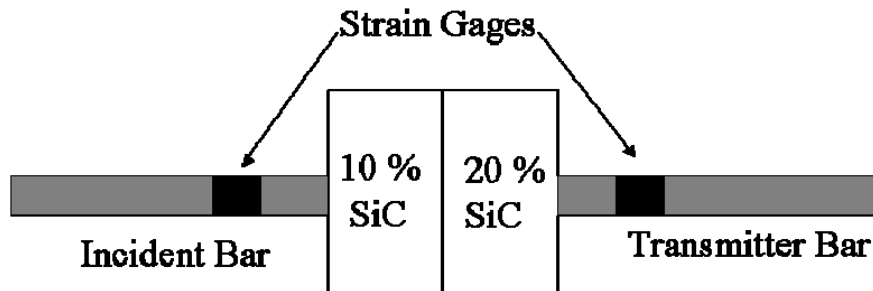
Figure 5.52 Schematic representation of the high strain rate test.

The model results also show good accordance with the observed failure of the first layer interfaces in layered samples. The relatively high compressive stresses result in larger discrepancies in the lateral displacements between the layers. This results in the separation of the interface.

CHAPTER 7

CONCLUSIONS

In this study, FGM systems composing of SiC-particulate Al composites of varying reinforcement volume fractions and single layer composites were manufactured by following a powder metallurgical route. Relative densities of the cold compacted samples were further increased by applying quasi-static uniaxial compression test up to 60% strain at a strain rate of $1.7x \ 10^{-3} \ s^{-1}$. Except 20% SiC composite the relative densities of single layer and multi-layer samples were found to be higher than 98% after quasi-static testing. The quasi-statically deformed samples were then cut into square cross-section of 10mm length and compression tested at high strain rates using a compression type Split Hopkinson Pressure Bar (SHPB) set-up in order to determine the effects of strain rate and wave propagation on the deformation behavior of multi layer composite samples. One of the material system composing of 10 and 20% SiC particles was further modeled using LSDYNA 3 finite element model program in order to validate the experimental results and also to develop modeling strategies for the future investigations. Based on the experimental and modeling results, followings can be concluded.

1. The deformation behavior of layered material system was found to be quite complex due to the differences between the Poisson's ratios of the individual layers leading to non-homogeneous deformation of layers.

2. The true stress-strain curves of discretely layered samples at quasi-static strain rates can however be approximated by using the corresponding individual layer properties based on equal-stress method.

3. The deformation behavior of layered samples at high strain rates was complicated due to the complex wave propagation events between the layers and SHPB bars and sample as well.

4. Modeling of two layers composite material system showed that the layer of lower mechanical impedance showed a higher stress-time history than the layer of higher impedance. The model results showed a good agreement with those of experimental results since the multi layer material systems tested failed particularly at the interface of the lowest

impedance layer. The failure occurred as the separation of the interface layer between the layers.

5. Microscopic observations have further shown that during processing of layered MMC samples, a thin oxide layer formed between the layers. The formation of thin oxide layer was expected to be a dominant factor in reducing the bonding strength between the layers.

6. In order to prevent oxide formation and hence to provide higher bonding strength between layers melting processes like slip casting, centrifugal casting or infiltration may be more appropriate than the powder metallurgical route.

7. The results shown in this study were preliminary and forming a basis for the future studies of wave propagation effects through the NSF/TUBİTAK project called Wave Propagation in Multi Layer Materials.

REFERENCES

[1] A. Kawasaki and R. Watanabe, "Concept and P/M fabrication of functionally gradient materials," *Ceramics International* **23**, (1997), 73.

[2] R. Roop Kumar and M.Wang, "Functionally graded bioactive coatings of hydroxyapatite / titanium oxide composite system," *Materials Letters* **3466,** (2002), 133.

[3] M. Krumova, C. Klingshirn, F. Haupert, K. Friedrich, "Microhardness studies on functionally graded polymer composites," *Composites Science and Technology* **61,** (2001), 557.

[4] K. Iwasaki, "Production of a functionally graded artificial tooth root by unique sequence of processes," *Materials Research Innovative* **1,** (1997), 180.

[5] A. Moro, Y. Kuroda, K. Kusaka, "Development status of the reusable high-performance engines with functionally graded materials," *Acta Astronautica* **50**, (2002), 427.

[6] S. C. Ernest Chin, "Army focused research team on functionally graded armor composites," *Materials Science and Engineering* **A259,** (1999), 155.

[7] M. L. Wilkins, "Mechanics of penetration and perforation," *International Journal of Engineering Science* **16**, (1978), 793.

[8] R. Watanabe, "Powder processing of functionally gradient materials," *Materials Research Science Bulletin*, January 1995.

[9] R. E. Mistler, V. K. Sikka, C. R. Scorey, J. E. McKernan, M. R. Hajaligol, " Tape casting as a fabrication process for iron aluminide (FeAl) thin sheets," *Materials Science and Engineering* **A258**, (1998), 258.

[10] M. N. Rahaman, R. E. Dutton, S. L. Semiatin, "Fabrication of dense thin sheets of γ-TiAl by hot isostatic pressing of tape-cast monotapes," *Materials Science and Engineering* **A360,** (2003), 169.

[11] Y. Zhang, J.Han, X. Zhang, X. He, Z. Li, S. Du, "Rapid prototyping and combustion synthesis of TiC/Ni functionally gradient materials," *Materials Science and Engineering* **A299**, (2001), 218.

[12] A. Ruder, H.P. Buchkremer, H. Jansen, W. Mallener, D. Stöver, "Wet powder spraying, a process for the production of coatings," *Surface Coatings Technology* **53**, (1992), 71.

[13] K. J. Jakubenas, J. M. Sanchez, H. L. Marcus, "Multiple material solid free-form fabrication by selective area laser deposition," *Materials & Design* **19**, (1998), 11.

[14] T. R. Jackson, H. Liu, N. M. Patrikalakis, E. M. Sachs, M. J. Cima, "Modeling and designing functionally graded material components for fabrication with local composition control," *Materials & Design* **20**, (1999), 63.

[15] B. Kieback, A. Neubrand, H. Riedel, "Processing techniques for functionally graded materials," *Material Science and Engineering* **A362**, (2003), 81.

[16] A. J. Ruys, E. B. Popov, D. Sun, J. J Russel, C. C. J. Murray, "Functionally graded electrical/thermal ceramic systems," *Journal of the European Ceramic Society* **21,** (2001), 2025.

[17] P. M. Biesheuvel, V. Breedveld, A. Higler, H. Verweij, "Graded membrane supports produced by centrifugal casting of a slightly polydisperse suspension," *Chemical Engineering Science* **56**, (2001), 3517.

[18] S. Put, J. Vleugels, O. Van der Biest, "Functionally graded WC–Co materials produced by electrophoretic deposition," *Scripta Materialia* **45**, (2001), 1139.

[19] J. S. Moya, A. J. Sanches-Herencia, J. Requena, R. Moreno, "Functionally graded ceramics by sequential slip casting," *Materials Letters* **14**, (1992), 333.

[20] J. Zhang, Y. Wang, B. Zhou, X. Wu, "Functionally graded Al/ Mg_2Si in-situ composites, prepared by centrifugal casting," *Journal of Materials Science Letters* **17**, (1998), 1677.

[21] Y. Watanabe, H. Eryu, K. Matsuura, "Evaluation of three-dimensional orientation of Al_3Ti platelet in Al-based functionally graded materials fabricated by a centrifugal casting technique," *Acta Materialia* **49**, (2001), 775.

[22] Y. Watanabe, N. Yamanaka, Y. Fukui, "Control of composition gradient in a metal-ceramic functionally graded material manufactured by the centrifugal method," *Composites Part A* **29,** (1998), 595.

[23] K. Arata, M. Yoshinaka, K. Hirota, and O. Yamaguchi, "Fabrication and mechanical properties of continuously graded $Wsi_2 - ZrO_2$ (2Y) materials using wet-molding," *Materials Research Bulletin* **33**, (1998), 627.

[24] M. P. Dariel, L. Levin, N. Frage, "Graded ceramic performs: various processing approaches," *Materials Chemistry and Physics* **67**, (2001), 192.

[25] S. F. Corbin, X. Zhao-jie, H. Henein, P. S. Apte, "Functionally graded metal/ceramic composites by tape casting, lamination and infiltration," *Materials Science and Engineering* **A262**, (1999), 192.

[26] S. Pratapa, I. M. Low, "Infiltration-processed, functionally graded aluminium titanate / zirconia-alumina composite," *Journal of Materials Science* **33**, (1998), 3047.

[27] S. Sampath, H. Herman, N. Shimoda, T. Saito, "Thermal spray processing of FGMs," *Materials Research Bulletin*, January 1995.

[28] Y. Y. Yang, "Time-dependent stress analysis in functionally graded materials," *International Journal of Solids and Structures* **37**, (2000), 7593.

[29] S. Schmauder, U. Weber, "Modelling of functionally graded materials by numerical homogenization," *Archive of Applied Mechanics* **71**, (2001), 182.

[30] Y. M. Shabana, N. Noda, "Thermo-elasto-plastic stresses in functionally graded materials under consideration of the fabrication process," *Archive of Applied Mechanics* **71**, (2001), 649.

[31] E. Weissenbek, H. E. Pettermann, S. Suresh, "Elasto-plastic deformation of compositionally graded metal-ceramic composites," *Acta Materialia* **45**, (1997) 3401.

[32] M. A. Meyers, *Dynamic Behavior of Materials*, (Wiley, New York, 1994), p. 27, 31.

[33] M. Lee, Y. H. Yoo, "Analysis of ceramic / metal armour systems," *International Journal of Impact Engineering* **25**, (2001), 819.

[34] S. Mahdi, B. A. Gama, S. Yarlagadda, J. W. Gillespie Jr., "Effect of the manufacturing process on the interfacial properties and structural performance of multi-functional composite structures," *Composites Part A* **34**, (2003), 635.

[35] D. P. Gonçalves, F. C. de Melo, A. N. Klein, H. A. Al-Qureshi, "Analysis and investigation of ballistic impacts on ceramic/metal composite armor," *International Journal of Machine Tools & Manufacture* **44**, (2004), 307.

[36] Y. M. Gupta and J. L. Ding, "Impact load spreading in layered materials and structures: concept and quantitative measure," *International Journal of Impact Engineering* **27**, (2002), 277.

[37] R. A. W. Mines, "A one-dimensional stress wave analysis of lightweight composite armour," *Composite Structures* **64**, (2004), 55.

[38] A. B. Hugh, "A one dimensional model for designing functionally graded materials to manage stress waves," *International Journal of Solids and Structures* **37**, (2000), 6383.

[39] Y. Li, K. T. Ramesh, E. S. C. Chin, "Dynamic characterization of layered and graded structures under impulsive loading," *International Journal of Solids and Structures* **38**, (2001), 6045.

[40] L. Banks-Sills, R. Eliasi, Y. Berlin, "Modeling of functionally graded materials in dynamic analyses," *Composites Part B* **33**, (2002), 7.

[41] M. H. Santare, P. Thamburaj, G. A. Gazonas, "The use of graded finite elements in the study of elastic wave propagation in continuously nonhomogeneous materials," *International Journal of Solids and Structures* **40**, (2003), 5621.

[42] M. Gasik, "Micromechanical modeling of functionally graded materials," *Computational Materials Science* **13**, (1998), 42.

[43] J. Hopkinson, "On the rupture of an iron wire by a blow," *J. Proc. Manchest. Liter. Philos. Soc.* **11,** (1872), 40.

[44] J. Harding, E.D. Wood, J.D. Campbell, "Tensile testing of materials at impact rates of strain," *Journal of Mechanical Engineering Science* **2,** (1960), 88

[45] J. Duffy, J.D. Campbell, R.H. Hawley, "On the use of a torsional split hopkinson bar to study rate effects in 1100-0 aluminium," *Journal of Applied Mechanics* **38,** (1971), 83.

[46] S. Nemat-Nasser, J.B. Isaacs, J.E. Starrett, "Hopkinson techniques for dynamic recovery experiments," *Proceedings of the Royal Society London* **A435,** (1991), 371.

[47] F.G. Karl, in *Wave Motion in Elastic Solids,* (Dover Publications, New York, 1975).

[48] R. J. Arsenault, in *Metal Matrix Composites: Mechanisms and Properties*, edited by R. K. Everett and R.J. Arsenault, (Academic Press, London, 1991).

[49] T. W. Clyne and P. J. Withers, in *An Introduction to Metal Matrix Composites*, (Cambridge University Press, Cambridge, 1993).

[50] F. J. Humphreys, in *9th. Ris International Symposia on Material Science*, edited by N. Andersen, (Ris National Lab., Denmark, 1988), p. 51.

[51] R. Dowling, J. Harding and J. D. Campbell, "The dynamic punching of metals," *Journal of the Institute of Metals* **98**, (1970) p. 215.

[52] P. S. Follansbee, in *Metallurgical Applications of Shock Wave and High-Strain Rate Phenomena*, edited by Marcel Dekker (L. E. Murr, K. P. Staudhammer and M. A. Meyers, Eds., New York, 1986), p. 451.

[53] Y. Li, K. T. Ramesh, "Influence of particle volume fraction, shape, and aspect ratio on the behavior of particle-reinforced metal–matrix composites at high rates of strain," *Acta Metallurgica et Materialia* **46**, (1998), 5633.

[54] W. G. Ferguson, A. Kumar, J. E. Dorn, *Journal of Applied Physics* **38,** (1967), 1836.

[55] J. Harding and M. Taya, *Proceedings of 6th International Conference On Composite Materials*, (Elsevier Applied Science, London, 1987), p. 376.

[56] A. Marchand, J. Duffy, T. A. Christman, S. Suresh, "An experimental study of the dynamic mechanical properties of an Al-SiC$_w$ composite**,"** *Engineering Fracture Mechanics* **30**, (1988), 295.

[57] C. C. Perng, J. R. Hwang, J. L. Doong, "High strain rate tensile properties of an (Al$_2$O$_3$ particles)-(Al alloy 6061-T6) metal matrix composite,"*Material Science and Engineering* **A171**, (1993), 213.

[58] S. I. Hong, G. T. Gray, *Journal of Materials Science* **29,** (1994), 2987.

[59] S. Yadav, D. R. Chichili, K. T. Ramesh, "The mechanical response of a 6061-T6 Al/Al$_2$O$_3$ metal matrix composite at high rates of deformation**,"** *Acta Metallurgica et Materialia* **43**, (1995), 4453.

[60] D. R. Chichili, K. T. Ramesh, "*Dynamic failure mechanisms in a 6061-T6 Al/Al$_2$O$_3$ metal-matrix composite***,"** *International Journal of Solids and Structures* **32**, (1995), 2609.

[61] M. Guden, I. W. Hall, "Quasi-static and dynamic compression behavior of an FP alumina reinforced aluminum metal matrix composite," *Journal of Material Science* **33**, (1998) 3285.

[62] G. Bao, Z. Lin, "*High strain rate deformation in particle reinforced metal matrix composites***,"** *Acta Metallurgica et Materialia* **44**, (1996), 1011.